



RESEARCH

# Interaction between Anderson and nonlinear localization in a forced and mistuned cyclic chain of oscillators with vibro-impact nonlinear energy sinks

Tobias Weidemann<sup>1</sup> · Lawrence A. Bergman<sup>2</sup> · Alexander F. Vakakis<sup>2</sup> · Malte Krack<sup>1</sup>

Received: 13 October 2025 / Revised: 19 March 2026 / Accepted: 23 April 2026  
© The Author(s) 2026

## Abstract

Random mistuning is widely known to lead to strong localization of vibrations in weakly-coupled, rotationally periodic structures composed of a finite number of sectors, which is known as Anderson localization. In the case of forced vibrations, this is typically associated with spatially confined large amplitude magnifications compared to the tuned system's resonant response. In addition to Anderson localization, strong localization effects can also occur in tuned but nonlinear rotationally periodic structures. In this work, we investigate the interaction between Anderson localization and nonlinear localization in a mistuned and harmonically forced cyclic chain of oscillators which incorporates internal strongly nonlinear devices for vibration mitigation, called vibro-impact nonlinear energy sinks (VI-NESs). A VI-NES consists of a small mass that is placed inside a cavity in each sector's primary mass where it undergoes dissipative (inelastic) impacts with the cavity walls. The tuned version of the studied system was recently shown to exhibit strong nonlinear localization effects due to Chimera-like steady-state vibrations in which sustained 1:1 resonance captures between the VI-NESs and their host oscillators occur in only a subset of all sectors. In the present work, we show both analytically and numerically that Anderson localization can constructively interact with the system's nonlinearly localized solutions by increasing both their amplitude and localization level, as well as by creating solution branches in parameter regions where the nonlinearly localized solution would not exist in the tuned configuration. Despite this strong interaction, the VI-NESs are still capable of effectively mitigating the vibrations of the chain. The implications of the findings of this work for real rotationally periodic engineering systems with VI-NESs are discussed.

**Keywords** Vibro-impact nonlinear energy sink · Rotationally periodic structures · Mistuning · Disorder · Vibration mitigation · Nonlinear localization · Anderson localization · Targeted energy transfer · Chimeras

## List of Abbreviations

|              |                                      |               |                                    |
|--------------|--------------------------------------|---------------|------------------------------------|
| <b>CM</b>    | Clearance mistuning                  | <b>LSR</b>    | Locally synchronized response      |
| <b>CX-A</b>  | Complexification-averaging           | <b>MCS</b>    | Monte-Carlo simulation             |
| <b>EM</b>    | Eigenfrequency mistuning             | <b>MDE</b>    | Measure differential equation      |
| <b>EOM</b>   | Equation of motion                   | <b>NES</b>    | Nonlinear energy sink              |
| <b>FRS</b>   | Frequency response surface           | <b>RMS</b>    | Root-mean-square                   |
| <b>GSR</b>   | Globally synchronized response       | <b>SIM</b>    | Slow invariant manifold            |
| <b>HB</b>    | Harmonic balance                     | <b>SMR</b>    | Strongly modulated response        |
| <b>IMTET</b> | Inter-modal targeted energy transfer | <b>TET</b>    | Targeted energy transfer           |
| <b>LF</b>    | Localization factor                  | <b>VI-NES</b> | Vibro-impact nonlinear energy sink |

✉ Tobias Weidemann  
tobias.weidemann@ila.uni-stuttgart.de

<sup>1</sup> University of Stuttgart, Stuttgart, Germany

<sup>2</sup> University of Illinois Urbana-Champaign, Urbana and Champaign in east-central Illinois, USA

## 1 Introduction

Periodic (or phononic) structures consist of (nearly) identical sectors (often called unit cells) that are coupled to each other in the form of a chain or a lattice. They are typically known for

their unique vibrational properties that can either be desired, e. g., as in meta-materials [1, 2], or simply be a side-effect of a structure's inherent, rotationally symmetric design, e. g., as in satellite antennas [3] or bladed disks in turbomachinery [4]. In (weakly non)linear but ideally periodic structures, i. e., structures with *perfectly identical* sectors, the modes take on the special form of harmonic plane waves. A plane wave is characterized as a state in which each sector undergoes the same periodic oscillation that is simply shifted in phase, relative to the oscillation of the neighboring sectors. Thereby, the eigenfrequencies of the plane wave modes and their corresponding inter-sector phase shifts, which can equivalently be expressed in terms of wavenumbers, are related through the structure's dispersion relation [2]. However, periodic structures can also be prone to energy localization. In the present work, we study the interaction between two distinct localization mechanisms, namely Anderson localization and nonlinear localization, in a rotationally periodic (cyclic) chain of oscillators, incorporating strongly nonlinear devices called vibro-impact nonlinear energy sinks (VI-NESs). In the following, we attempt to provide an overview of Anderson and nonlinear localization, as well as the working principle of VI-NESs and their use for vibration mitigation in non-periodic and rotationally periodic structures.

## 1.1 Anderson localization

In ideally periodic structures, all sectors have identical *local eigenfrequencies*. Throughout this work, we use the term “local eigenfrequencies” to refer to the eigenfrequency(ies) of isolated (uncoupled) sectors. This matching of local eigenfrequencies creates a 1:1(:...:1) resonance condition among all sectors and allows them to efficiently exchange energy across the structure. In the presence of small random perturbations to any of the sectors' parameters, however, this resonance condition is broken and energy can become trapped in space. We refer to such random perturbations as mistuning (also called disorder) and call localization due to mistuning *Anderson localization*, after being first discovered by P. W. Anderson [5]. From a modal perspective, mistuning makes the structure's modes lose their plane wave character and causes them to become spatially localized instead [6, 7]. Thereby, the intensity of mode localization was found to be mainly governed by the ratio between the inter-sector coupling strength and the mistuning level [8]. In the case of resonant forced vibrations, Anderson localization is associated with large amplitude magnifications compared to the resonant response of the tuned system [9]. For weak but non-zero mistuning levels (or mistuning intensities) there exists a “sweet spot” at which the amplitude magnifications reach a maximum [10]. As mistuning is almost inevitable in practice due to effects like material imperfections or manufacturing tolerances, Anderson localization can be of high relevance in

engineering applications. A prominent example for the latter is mistuning of bladed disks in turbomachinery [11–13].

If (strong) nonlinearities are present in a mistuned system, its response was shown to de-localize compared to the mistuned linear(ized) case [14]. The combined effect of mistuning and nonlinearity inevitably receives great interest in the design of mistuned bladed disks where various sources of strong nonlinearities can be present, e. g., due to contact interactions in mechanical joints [15–17]. In the study by Petrov and Ewins [18], a mistuned bladed disk with under-platform friction dampers and shroud contacts was considered. They found that mistuning of the nonlinear parameters leads to smaller localization effects than mistuning of the linear parameters that directly influence the bladed disk's linear modes. Other studies from the field of turbomachinery found that deliberately introducing nonlinearities, such as piezoelectric shunt circuits [19] or ring friction dampers [20], has the potential to significantly reduce the maximum mistuned vibration levels compared to the linear mistuned response. Yet it was also shown in [21], for the example of blade-casing interactions, that nonlinear systems may experience higher amplitude *magnifications* than linear systems, which is the ratio between the mistuned maximum vibration level and the tuned maximum vibration level. However, it should be noted that the amplitude magnification in nonlinear systems does not only depend on the mistuning level but also on the forcing level, i. e., the energy level of the forced vibration. This was clearly demonstrated in [22] for a geometrically nonlinear bladed disk, which exhibits an isolated frequency-amplitude curve for low excitation levels that merges with the main frequency-amplitude curve at large excitation levels. While the reported amplitude magnifications in [22] exceeded those of the corresponding linear systems in the range of forcing amplitudes where the isolated frequency-amplitude curve exists, they were significantly lower after the isolated branch fully merged with the main frequency-amplitude curve.

## 1.2 Nonlinear localization

In addition to Anderson localization, localization effects are also known to occur in perfectly periodic (tuned) but nonlinear structures [23–26], which was first discovered by A. J. Sievers and S. Takeno [27]. Intuitively, *nonlinear localization* can be understood as a form of effective mistuning introduced by the nonlinearity: as the nonlinear local eigenfrequency of each sector is dependent on its energy level [28], the sectors lose the internal 1:1 resonance condition if the energy level differs among the sectors [29]. From the perspective of nonlinear mode theory, nonlinear localization [30] can be explained by the localization of the structure's modes. Here it was shown by Vakakis et al. [24, 30] that the ratio between the inter-sector coupling strength and the nonlinearity determines the intensity of localization in these

modes. As the change of the sectors' local eigenfrequencies with their energy level is governed by how strong the nonlinearity is, the latter can be interpreted as being equivalent to the mistuning level in the case of Anderson localization.

Takeno and Homma [31] showed that nonlinearly localized solutions are robust in the presence of mistuning, meaning that a nonlinearly localized solution of an initially tuned system may still exist when mistuning is introduced. Throughout the literature, however, most studies focus on either Anderson localization or nonlinear localization, but to date there is almost no detailed study concerning the potential interactions between both effects. To the best of the authors' knowledge, only King and Layne [32] studied the nonlinear normal modes in a nonlinear rotationally periodic system with mistuning. They found that non-localized and weakly localized nonlinear modes cease to exist as the ratio between the mistuning level and nonlinearity increases, thus only leaving strongly localized modes. Hence, in contrast to the aforementioned de-localizing effect of nonlinearities on Anderson localization, one can also obtain an opposite amplifying effect when Anderson and nonlinear localization constructively interact with each other.

### 1.3 Nonlinear energy sinks

VI-NESs, as considered in the present work, belong to the wider class of nonlinear energy sinks (NESs). NESs are passive nonlinear vibration absorbers that consist of a small mass which is attached to a host structure in an essentially (or nearly essentially) nonlinear, i. e., non-linearizable, way. In a VI-NES, the essentially nonlinear coupling is realized by freely placing the small mass in a cavity inside the host structure, where it undergoes impacts with the cavity walls (free-play nonlinearity). Other common coupling nonlinearities employed in NESs include cubic springs [33, 34], rotational inertia coupling [35, 36], bi-stable elements [37, 38], constraint motion on tracks [39, 40], and combinations of those [41]. The essentially nonlinear coupling allows NESs to engage into transient or sustained 1:1 (or even 1:2, 2:1, etc.) resonance captures [42] with the host structure at theoretically arbitrary frequencies. These resonance captures open channels for *targeted energy transfer* (TET) from the host structure into the NES [29] where the energy is then localized and ultimately dissipated. Thereby, NESs offer a significant advantage over classical linear tuned mass dampers where TET is only possible in a very narrow frequency band to which the tuned mass damper's parameters are tuned [43]. The effectiveness of NESs, however, is typically limited by the energy level of the host structure, to which tuned mass dampers are invariant. To overcome this limitation of NESs, recent research has focused on hybrid approaches by implementing an additional linear coupling between the host structure and the NES that allow the latter

to function as a tuned mass damper at low energy levels and a pure NES at high energy levels [44].

#### 1.3.1 Working principle of VI-NESs in non-periodic structures

The high efficacy of VI-NESs for vibration mitigation in non-periodic structures was already shown for random excitation [45, 46], impulsive/seismic excitation [47, 48], and harmonically forced vibrations [49, 50]. In the present work, we focus on the latter. If the host structure is harmonically forced, two dynamic regimes are known to occur, depending on the ratio between the host structure's amplitude at the location of the VI-NES and the clearance between the VI-NES and the cavity walls [51]. When this ratio is small, the dynamics of the VI-NES can only engage into *transient* 1:1 resonance captures with the host structure, and the latter undergoes a strongly modulated response (SMR). For large ratios, on the other hand, the dynamics of the VI-NES engage into a *sustained* 1:1 resonance capture with the host structure during which the motions of the cavity walls and the VI-NES are synchronized. It was concluded in [52] that TET during a sustained 1:1 resonance capture is maximized when two symmetric impacts per period occur, for which a representative example of the VI-NESs motion (red) between the cavity walls (blue) is shown at the top in Fig. 1. Besides resonant TET from the host structure to the VI-NES, it has also been shown that the VI-NES can induce a strong and rapid redistribution (scattering) of energy within its host structure's modal space, known as inter-modal TET (IMTET) [29, 53]. In fact, VI-NESs can be designed to solely rely on IMTET, thus, achieving a strong vibration mitigation effect by exploiting the inherent damping capacity of the host structure's higher modes [50]. However, a possible limitation of intense IMTET might be its influence of the internal stress level of the host structure, which has been shown to increase in some cases in [46]. The recent study by Gzal et al. [54] suggests another interpretation of the working principle of VI-NESs from the perspective of *energy management*; due to the VI-NES's strong influence on the host structure's motion, it may effectively reduce the input energy that enters into the host structure from the external forcing.

#### 1.3.2 Application of VI-NESs to tuned rotationally periodic structures

The effects of VI-NESs in a tuned rotationally periodic structure under symmetric harmonic standing or traveling wave forcing were recently studied by Weidemann et al. [55]. They considered a cyclic chain of oscillators in which each sector consists of a single oscillator that is linearly coupled to the ground and to its nearest neighboring sectors, and further hosts a VI-NES. The system was shown to exhibit a *globally*

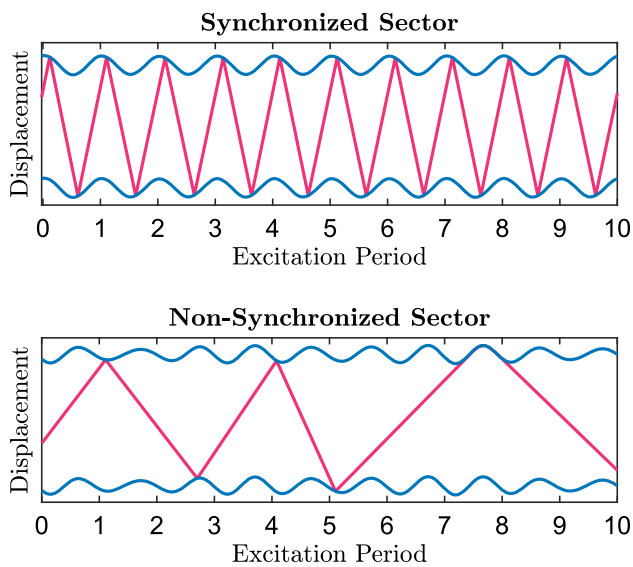


**Fig. 1** Motion of the VI-NES (red) between its bounding cavity walls (blue) in a synchronized and a non-synchronized sector during the same time interval of a representative locally synchronized response (LSR)

*synchronized response* (GSR) during which a sustained 1:1 resonance capture between the host oscillator and its VI-NES occurs in every sector, and the global motion of the system takes on the form of a harmonic plane wave with the same wavenumber as that of the excitation. If the ratio between the host oscillator's amplitude and the clearance of the VI-NES is too small to support these sustained 1:1 resonance captures, each sector tends to exhibit a SMR. In this case, the VI-NESs induce strong IMTET among the host structure's modes that possess different wavenumbers. Even though the response is then no longer a plane wave, the system's energy remains evenly distributed among the sectors in the long-term average sense.

In addition to GSRs, it was found in [55] that sustained 1:1 resonance captures between the host oscillators and their VI-NESs can also occur in only a (proper) subset of sectors. This is referred to as a *locally synchronized response* (LSR). In the other non-synchronized sectors, the VI-NESs' motions are irregular and impacts occur only rarely. A representative example of the VI-NES's motion between the cavity walls in a synchronized and a non-synchronized sector is shown in Fig. 1. We note that LSRs may thus be interpreted as a type of Chimera state which are known to occur in systems consisting of coupled identical oscillators [56, 57]. Even though there exists no unified definition of a Chimera state, as pointed out in the review by Haugland [58], the term is commonly used to refer to a state in which some oscillators exhibit a coherent or synchronized response, while the remaining ones exhibit an incoherent or non-synchronized response. During an LSR, the amplitudes (and thus the energy) can strongly

vary among all sectors, meaning that LSRs are nonlinearly localized solutions of the system. It should be noted that the largest amplitudes of LSRs reported in [55] were still found to be lower than the host structure's linear resonant response where the masses of the VI-NESs are fixed in all sectors (no mass deficiency). However, their amplitudes largely exceed those of (non-localized) GSRs or SMRs if the inter-sector coupling strength is weak and the excitation wavenumber is low. Hence, it is clear that a deeper understanding of LSRs is required for the robust design of VI-NESs as a means for vibration mitigation of real rotationally periodic structures, which are, to a certain extent, always mistuned.

#### 1.4 Goal and structure of the present work

The goal of the present study is to assess how Anderson localization due to mistuning interacts with LSRs, i.e., the Chimera-like nonlinearly localized solutions of a rotationally periodic structure that incorporates a distributed array of VI-NESs. To this end, we consider a mistuned modification of the minimal model of a rotationally periodic structure in the form of a cyclic chain of oscillators with VI-NESs, proposed by Weidemann et al. in [55]. It should be noted that cyclic chains of oscillators, as considered to be the host structure of the VI-NESs herein, are commonly used to qualitatively assess the effects of mistuning [6, 9] and nonlinear localization [25, 59] in real rotationally periodic engineering structures. Even though we focus on VI-NESs in particular, we expect the qualitative results obtained in the present work to be (to some extent) generalizable to other types of NESs applied to rotationally periodic structures, as we will discuss in more detail at the end of this article. To the best of the authors' knowledge, the present work is the first to explicitly consider the direct interaction between Anderson and nonlinear localization in a forced system. We address the aforementioned research question by applying and further extending some of the findings presented in the study on the tuned system [55]. To make the present article self contained, we will summarize these findings where deemed necessary.

The present article is organized as follows. The model of the proposed system and the considered sources of mistuning are introduced in Section 2. We then integrate mistuning into the analytical model of LSRs developed in [55] in Section 3 and utilize it to study the influence of mistuning to each sector's local eigenfrequency and clearance in Section 4 and Section 5, respectively. The article ends with a discussion of the results and conclusions in Section 6.

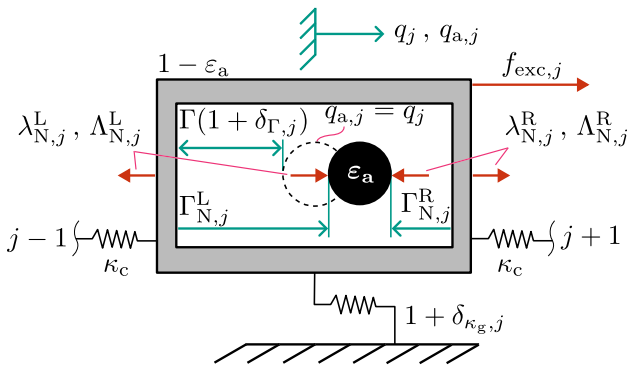


**Fig. 2** Sketch of a single sector  $j$  and definition of the dimensionless quantities

## 2 Problem setting

### 2.1 Description of the model

We consider a mistuned modification of the dimensionless model of a cyclic chain of oscillators that hosts a distributed array of VI-NESs derived by Weidemann et al. [55]. The cyclic chain has a total number of sectors,  $N_s$ , that are indexed within  $j \in \{1, \dots, N_s\}$ . A sketch of a single sector  $j$  together with a definition of the dimensionless quantities can be found in Fig. 2. Each sector contains a single oscillator whose displacement and velocity are denoted by  $q_j$  and  $u_j$ , respectively. The oscillator is linear-elastically coupled to the oscillators of its two nearest neighboring sectors by the stiffness  $\kappa_c$  and to the ground by the stiffness  $1 + \delta_{\kappa_g,j}$ . We consider  $\delta_{\kappa_g,j}$  to be a relative mistuning with respect to the nominal grounding stiffness of unity. Each oscillator further hosts a VI-NES with small mass  $0 < \varepsilon_a \ll 1$ . To ensure that no mass deficiency is introduced between the system with VI-NESs and the corresponding system with no VI-NESs, obtained in the limit  $\varepsilon_a \rightarrow 0$ , we assume that the sector (VI-NES plus host oscillator) always has a total and constant unit mass 1. The dimensionless mass of the VI-NES,  $\varepsilon_a$ , thus directly determines the mass ratio between the VI-NES and the entire sector. The coordinate of the VI-NES  $q_{a,j}$ , with respective velocity  $u_{a,j}$ , counts in the inertial reference frame, and is zero when  $q_j = 0$  and the VI-NES is located at the center of the cavity (dashed circle in Fig. 2).

In each sector, we model the contacts between the VI-NES and the left and right cavity walls of its host oscillator in the form of unilateral constraints in combination with the generalized form of Newton’s impact law. This approach allows for impulsive phases that cannot be accounted for by ordinary differential equations, as these do not capture instantaneous changes of the system’s velocities. In order to treat the resulting non-smoothness in the system’s dynamics in a mathematically rigorous way, we formulate the equations of motions (EOMs) as *measure differential equations*

(MDEs). This formalism of describing non-smooth systems was first proposed by Moreau [60]. We refer the reader who might not be familiar with the theory behind MDEs to the book by Glocker [61]. The resulting MDEs that govern the EOMs of the host oscillator and the VI-NES are read as:

$$(1 - \varepsilon_a)du_j + (q_j (1 + \delta_{\kappa_g,j}) + \kappa_c (2q_j - q_{j-1} - q_{j+1}) + \sum_{m=1}^{N_s} c_{jm}u_m) d\tau + (d\Pi_j^L - d\Pi_j^R) = f_{exc,j}d\tau, \tag{1}$$

$$\varepsilon_a du_{a,j} - \underbrace{(d\Pi_j^L - d\Pi_j^R)}_{=:d\Pi_j} = 0. \tag{2}$$

Herein,  $d\Box$  denotes the *measure* of the respective quantity and  $\tau$  denotes time. In Eq. (1), we further introduced the general form of a viscous damping term with coefficients  $c_{jm}$  that is not explicitly shown in Fig. 2. The measures of the contact percussions  $d\Pi_j^{L,R} = \lambda_{N,j}^{L,R}d\tau + \Lambda_{N,j}^{L,R}d\eta$ , where the superscripts L and R denote left and right cavity walls, respectively, combine the smooth contact forces  $\lambda_{N,j}^{L,R}$  over  $d\tau$  and the impulsive contact reactions  $\Lambda_{N,j}^{L,R}$  over the atomic measure  $d\eta$ . The latter is defined as the sum of Dirac measures at every impulsive time instant and can be interpreted to act as a sequence of Dirac impulses. Further, all oscillators are subjected to an external harmonic forcing  $f_{exc,j}(\tau)$  of standing/traveling wave form and an amplitude of unity:

$$f_{exc,j}(\tau) = \text{Re} \left\{ e^{i\theta_{k_0}(j-1)} e^{ir\tau} \right\}. \tag{3}$$

Herein,  $i = \sqrt{-1}$  is the imaginary unit,  $\text{Re} \{ \Box \}$  refers to the real part of the complex number, and  $r$  is the forcing frequency. Moreover,  $\theta_{k_0} = 2\pi k_0/N_s$  describes the inter-sector phase angle of the forcing with integer wavenumber  $k_0$ .

The smooth contact forces and the unilateral constraints at the left and right cavity walls must fulfill the following complementarity conditions known as Signorini’s law:

$$0 \leq \lambda_{N,j}^L \perp \Gamma_{N,j}^L (q_j, q_{a,j}) \geq 0, \quad \Gamma_{N,j}^L = \Gamma (1 + \delta_{\Gamma,j}) - (q_j - q_{a,j}), \tag{4}$$

$$0 \leq \lambda_{N,j}^R \perp \Gamma_{N,j}^R (q_j, q_{a,j}) \geq 0, \quad \Gamma_{N,j}^R = \Gamma (1 + \delta_{\Gamma,j}) + (q_j - q_{a,j}). \tag{5}$$

Herein,  $\Gamma_{N,j}^L$  and  $\Gamma_{N,j}^R$  are the signed contact distances corresponding to the left and right cavity walls, respectively. The VI-NES is in contact with the respective cavity wall if either one of  $\Gamma_{N,j}^{L,R}$  is zero (closed contact). The orthogonality symbol  $\perp$  in Eqs. (4) and (5) states that only then, a

repelling contact force  $\lambda_{N,j}^{L,R} \geq 0$  can act to enforce the condition  $\Gamma_{N,j}^{L,R} \geq 0$ , i.e., to avoid interpenetration. Both  $\Gamma_{N,j}^{L,R}$  depend on the size of the clearance  $\Gamma(1 + \delta_{\Gamma,j})$ , which is defined as the symmetric distance between the VI-NES and each cavity wall when the VI-NES is located at the center of the cavity,  $q_{a,j} = q_j$ . The clearance can be decomposed into its nominal value  $\Gamma$ , which is the same in each sector, and the sector-specific relative mistuning  $\delta_{\Gamma,j}$ . An impact occurs if a contact is closed with non-zero relative velocity. As mentioned above, we treat these events with the generalized form of Newton’s impact law. The latter gives a condition for the impulsive contact reactions  $\Lambda_{N,j}^{L,R}$  that can be formulated in terms of the following complementarity conditions:

$$0 \leq \Lambda_{N,j}^L \perp e_N (u_{a,j} - u_j)^- + (u_{a,j} - u_j)^+ \geq 0, \quad (6)$$

$$0 \leq \Lambda_{N,j}^R \perp e_N (u_j - u_{a,j})^- + (u_j - u_{a,j})^+ \geq 0. \quad (7)$$

These conditions depend on the relative pre- and post-impact velocities,  $(\square)^-$  and  $(\square)^+$ , as well as the coefficient of restitution  $e_N$ . The impact is energy conserving (elastic) for  $e_N = 1$  and dissipative (inelastic) for  $0 \leq e_N < 1$ .

To achieve *rotational* periodicity of this system, we introduce periodic boundary conditions, which couple the last sector of the chain  $j = N_s$  to the first sector  $j = 1$ :

$$[j-1] = \begin{cases} j-1 & \text{if } j > 1 \\ N_s & \text{if } j = 1 \end{cases}, \quad [j+1] = \begin{cases} j+1 & \text{if } j < N_s \\ 1 & \text{if } j = N_s \end{cases}. \quad (8)$$

The EOMs of all sectors can then be summarized in matrix form as

$$\mathbf{M} \mathbf{d} \mathbf{u} + (\mathbf{C} \mathbf{u} + (\mathbf{K} + \delta \mathbf{K}) \mathbf{q}) \, d\tau + d\mathbf{\Pi} = \text{Re}\{\hat{\mathbf{F}}_{k_0} e^{i r \tau}\} d\tau \quad (9)$$

$$\mathbf{M}_a \mathbf{d} \mathbf{u}_a - d\mathbf{\Pi} = \mathbf{0}. \quad (10)$$

Herein, we gather the displacements of the oscillators and the VI-NESs in the respective entries of the vectors  $\mathbf{q}$  and  $\mathbf{q}_a$  with corresponding velocities  $\mathbf{u}$  and  $\mathbf{u}_a$ . The diagonal mass matrices are given by  $\mathbf{M} = (1 - \varepsilon_a) \mathbf{I}$  and  $\mathbf{M}_a = \varepsilon_a \mathbf{I}$ , where  $\mathbf{I}$  is the  $N_s \times N_s$  identity matrix. The nominal stiffness matrix  $\mathbf{K}$  is of a circulant form [62] which is characteristic for rotationally periodic systems:

$$\mathbf{K} = \begin{bmatrix} 1 + 2\kappa_c & -\kappa_c & 0 & \dots & -\kappa_c \\ -\kappa_c & 1 + 2\kappa_c & -\kappa_c & \dots & 0 \\ 0 & -\kappa_c & 1 + 2\kappa_c & \ddots & \vdots \\ \vdots & \ddots & \ddots & \ddots & -\kappa_c \\ -\kappa_c & 0 & \dots & -\kappa_c & 1 + 2\kappa_c \end{bmatrix}. \quad (11)$$

The mistuning of the grounding stiffnesses is introduced by the diagonal stiffness mistuning matrix  $\delta \mathbf{K} = \text{diag}\{\delta_{\kappa_{g,j}}\}$ , the viscous damping coefficients  $c_{jm}$  are the entries of the

viscous damping matrix  $\mathbf{C}$ , and the entries of the complex forcing amplitude vector  $\hat{\mathbf{F}}_{k_0}$  are defined as  $\hat{F}_{j,k_0} = e^{i\theta_{k_0}(j-1)}$ . Lastly, the vector of contact percussion measures  $d\mathbf{\Pi}$  holds the combined measures of the contact percussions at the left and right cavity walls,  $d\Pi_j$ , as defined in Eq. (2).

### 2.2 Linear dynamics of the host structure

The linear tuned configuration of the proposed system where the masses of the VI-NESs are fixed in all sectors, i.e., Eq. (9) with an identity mass matrix,  $\mathbf{M} = \mathbf{I}$ , no mistuning,  $\delta \mathbf{K} = \mathbf{0}$ , and deactivated contacts,  $d\mathbf{\Pi} = \mathbf{0}$ , will serve as a reference configuration throughout our study. In order to determine its linear modal basis, we momentarily assume the system to be conservative by further setting  $\mathbf{C} = \mathbf{0}$  and  $\hat{\mathbf{F}}_{k_0} = \mathbf{0}$ . In this case, the modes take on the form of discrete harmonic standing or traveling waves [2]. Their integer wavenumbers  $l$  lie within the modal wavenumber spectrum  $\mathcal{L}$  which depends on the number of sectors  $N_s$  and is given by

$$\mathcal{L} = \left\{ l \in \mathbb{Z} \mid -\left\lfloor \frac{N_s - 1}{2} \right\rfloor \leq l \leq \left\lfloor \frac{N_s}{2} \right\rfloor \right\}. \quad (12)$$

Therein,  $l = 0$  and  $l = N_s/2$  describe standing waves,  $l < 0$  indicate backward traveling waves, and  $0 < l < N_s/2$  indicate forward traveling waves. For each wavenumber, the corresponding eigenfrequency  $r_l$  can be obtained from the dispersion relation [62]:

$$r_l = \sqrt{1 + 4\kappa_c \sin^2\left(\frac{\theta_l}{2}\right)}. \quad (13)$$

Herein,  $\theta_l = 2\pi l/N_s$  is the inter-sector phase angle. Since Eq. (13) is symmetric around  $l = 0$ , all traveling wave modes with the same  $|l|$  also have the same eigenfrequency. This makes these mode pairs *degenerate*, meaning that their corresponding mode shapes can be arbitrarily chosen to form an orthogonal basis of generalized eigenvectors spanning their corresponding two-dimensional eigenspaces. Without loss of generality, we choose to define the mode shapes  $\varphi_l$  in the form of complex harmonic waves. The entries of the mass-normalized mode shape,  $\varphi_{j,l}$ , of wavenumber  $l$  at sector  $j$  and the corresponding modal transformation matrix  $\Phi_{\text{ref}}$  are then read as:

$$\varphi_{j,l} = \frac{e^{i\theta_l(j-1)}}{\sqrt{N_s}}, \quad (14)$$

$$\Phi_{\text{ref}} = \left[ \varphi_{-\lfloor \frac{N_s-1}{2} \rfloor} \cdots \varphi_{-\lfloor \frac{N_s}{2} \rfloor} \right]. \quad (15)$$

It should be noted that the mode shapes are mass-normalized with respect to the identity matrix  $\mathbf{M} + \mathbf{M}_a = \mathbf{I}$ . This results in

$\Phi_{\text{ref}}$  being unitary, i. e., its inverse is given by the Hermitian transpose  $\Phi_{\text{ref}}^{-1} = \Phi_{\text{ref}}^H$ . Assuming that the linear damping matrix  $\mathbf{C}$  is described by a modal damping of the tuned system’s modes with fixed VI-NESs in all sectors,  $\mathbf{C}$  is given by:

$$\mathbf{C} = \Phi_{\text{ref}} \text{diag} \left\{ 2D_{-\lfloor \frac{N_s-1}{2} \rfloor} r_{-\lfloor \frac{N_s-1}{2} \rfloor}, \dots, 2D_{\lfloor \frac{N_s}{2} \rfloor} r_{\lfloor \frac{N_s}{2} \rfloor} \right\} \Phi_{\text{ref}}^H. \tag{16}$$

Herein,  $D_l$  is the linear modal damping ratio of the mode with wavenumber  $l$ .

Projecting the excitation vector  $\hat{\mathbf{F}}_{k_0}$  onto the mode shape  $\varphi_l$  of the mode with wavenumber  $l$  yields

$$\varphi_l^H \hat{\mathbf{F}}_{k_0} = \begin{cases} \sqrt{N_s} & \text{if } l = k_0 \\ 0 & \text{if } l \neq k_0 \end{cases}. \tag{17}$$

This shows that only one tuned system mode is excited by the forcing. Due to the aliasing effect, the host structure always experiences an effective excitation with a wavenumber within  $\mathcal{L}$ , even if  $k_0$  would lie outside of  $\mathcal{L}$ . When further considering the reciprocity of the system, one can see that it is sufficient to study excitation wavenumbers within the symmetric positive half of  $\mathcal{L}$ , i. e.,  $k_0 \in \{k \in \mathcal{L} \mid k \geq 0\}$ . Under the assumption of light modal damping,  $0 < D_{k_0} \ll 1$ , the linear resonance amplitude of each oscillator,  $\hat{q}_{\text{ref}}$ , is given by

$$\hat{q}_{\text{ref}} = \frac{1}{2D_{k_0} r_{k_0}^2}. \tag{18}$$

The latter will serve as a reference for assessing the vibration levels observed in the analysis presented herein.

### 2.3 Mistuning configurations

Throughout this work, we consider two distinct sources of mistuning:

1. *eigenfrequency mistuning* (EM), which describes random perturbations to the linear local eigenfrequency of each sector, and
2. *clearance mistuning* (CM), which describes random perturbations to the size of the clearance in each sector,

While CM is directly introduced through the relative clearance mistuning  $\delta_{r,j}$ , EM requires further explanation. Therefore, we describe in the following how the latter is introduced into the system and how the effects of mistuning are quantified.

#### 2.3.1 Eigenfrequency mistuning

We motivate EM to directly describe a loss of the internal 1:1(: ... :1) resonance condition among all sectors of the host structure. As described in Section 1.1, this inhibits energy transfer across the chain and leads to Anderson localization. According to the EOM of a linear conservative isolated sector, i. e., Eq. (1) with  $\kappa_c = 0$ ,  $c_{jm} = 0$ ,  $d\Pi_j = 0$ , and  $f_{\text{exc},j} = 0$ , the linear local eigenfrequency of each sector can be determined as  $r_{\text{loc},j} = \sqrt{\frac{1+\delta_{\kappa_g,j}}{1-\varepsilon_a}}$ . We assume that  $\delta_{\kappa_g,j}$  is chosen in such a way that  $r_{\text{loc},j}$  has a relative frequency mistuning of  $\delta_{r,j}$  compared to the tuned local eigenfrequency, i. e.,  $r_{\text{loc},j} = (1 + \delta_{r,j})\sqrt{\frac{1}{1-\varepsilon_a}}$ . By equating these definitions of  $r_{\text{loc},j}$ , one can convert the relative local eigenfrequency mistuning  $\delta_{r,j}$  to a relative grounding stiffness mistuning  $\delta_{\kappa_g,j}$ :

$$(1 + \delta_{r,j})\sqrt{\frac{1}{1 - \varepsilon_a}} = \sqrt{\frac{1 + \delta_{\kappa_g,j}}{1 - \varepsilon_a}}, \tag{19}$$

$$\Leftrightarrow \delta_{\kappa_g,j} = 2\delta_{r,j} + \delta_{r,j}^2. \tag{20}$$

Linearizing the relationship in Eq. (20) yields the approximate relation  $\delta_{\kappa_g,j} \approx 2\delta_{r,j}$ . For the small mistuning considered in the present work, this shows that the mistuning level of the grounding stiffnesses is approximately twice as large as the mistuning level of the local eigenfrequencies. Throughout our studies the exact relation in Eq. (20) was used.

At this point it should be recalled that we defined the linear viscous damping matrix  $\mathbf{C}$  as a modal damping matrix of the tuned host structure (see Eq. (16)). However, as EM alters the grounding stiffnesses it also affects the host structure’s modes and, consequently, the linear damping matrix  $\mathbf{C}$  results in non-proportional damping in the presence of EM. While this may generally yield more complex dynamics due to the linear coupling of the host structure’s modes, we found no qualitative differences from the findings reported throughout the study when considering modal damping of the *mistuned* modes instead. This is because the VI-NESs dominate both the energy dissipation and the energy transfer among the modes, compared to the weak linear non-proportional damping considered in the present work (as defined in Section 2.5).

#### 2.3.2 Probability distribution function for random mistuning

For both EM and CM, we gather the respective *mistuning patterns*, i. e., the spatial distributions of  $\delta_{r,j}$  and  $\delta_{\Gamma,j}$ , in the vectors  $\boldsymbol{\delta}_r = [\delta_{r,1} \dots \delta_{r,N_s}]$  and  $\boldsymbol{\delta}_\Gamma = [\delta_{\Gamma,1} \dots \delta_{\Gamma,N_s}]$ , respectively. We assume their probability density function to be described by an uncorrelated multivariate normal dis-

tribution,  $\mathcal{N}(\delta, \sigma)$ , with zero mean and uniform standard deviation  $\sigma$ :

$$\mathcal{N}(\delta, \sigma) = \prod_{j=1}^{N_s} \frac{1}{\sigma\sqrt{2\pi}} e^{-\frac{1}{2}\left(\frac{\delta_j}{\sigma}\right)^2}. \quad (21)$$

All random samples of the mistuning patterns  $\delta_r$  and  $\delta_\Gamma$  are generated with a Mersenne Twister algorithm [63]. The seed of the algorithm is “randomly” chosen based on the current time at the initialization. For each sample drawn, we additionally subtract the mean value over all sectors to ensure that the sector average of the mistuned parameters corresponds to its nominal value, i. e.,  $\text{mean}_j \{\delta_j\} = 0$ . With this we aim to isolate mistuning effects from other effects that originate from variations of the respective (mean) nominal parameter value.

## 2.4 Numerical simulation and quantities of interest

All numerical simulations of the EOMs in Eqs. (9) and (10) are performed with the symmetric version of Moreau’s time stepping scheme [64]. Compared to event-driven techniques, Moreau’s time stepping scheme is able to overcome accumulation points, i. e., infinitely many events occurring in a finite amount of time (which typically happen in the transition towards sustained contact between a VI-NES and a cavity wall), and eliminates the need to determine every time instant in which an event occurs. Event-driven schemes are known to perform poorly in the presence of many (consecutive) events, which are expected for the cyclic chain of oscillators where many impacting bodies are involved. As suggested by a convergence study, the time step  $\Delta\tau$  is chosen so that each excitation period is sampled with 1000 steps, i. e.,  $\Delta\tau = 2\pi/(1000r)$ . Based on the system’s simulated response, we quantify the vibration level of each sector in terms of its mean amplitude over time,  $\hat{q}_j$ . The latter is determined by averaging half of the oscillator’s peak-to-peak displacement over all simulated excitation periods during a steady-state response. As a scalar measure of the system’s vibration level, we additionally introduce the maximum amplitude over all sectors,  $\hat{q}_{\max}$ , as:

$$\hat{q}_{\max} = \max_j \{\hat{q}_j\}. \quad (22)$$

To quantify the intensity of localization for a given spatial amplitude distribution, we utilize the localization factor (LF) as introduced in [65]. It is defined over the ratio between the maximum amplitude  $\hat{q}_{\max}$  and the root-mean-square (RMS) amplitude over all sectors, as:

$$\text{LF} = \frac{1}{\sqrt{N_s} - 1} \left( \frac{\hat{q}_{\max}}{\text{RMS}_j \{\hat{q}_j\}} - 1 \right). \quad (23)$$

The LF takes on a value of 0 if the amplitudes  $\hat{q}_j$  in all sectors are identical and 1 if the entire energy is localized in a single sector (in which case  $\text{RMS}_j \{\hat{q}_j\} = \hat{q}_{\max}/\sqrt{N_s}$ ).

As a means of determining which sectors are synchronized and which are not, based on the system’s numerically simulated response, we count the number of *significant* impacts per excitation period that occur in each sector,  $N_{\text{sipp},j}$ . A significant impact is herein defined as an impact during which the motion of the respective VI-NES reverses. Due to the sustained 1:1 resonance capture, a synchronized sector will theoretically always exhibit  $N_{\text{sipp},j} = 2$ , while a non-synchronized sector will exhibit less significant impacts per period, i. e.,  $N_{\text{sipp},j} < 2$  (cf. Fig. 1). To account for potential inaccuracies in the counting process, we set the boundary for synchronized sectors to  $N_{\text{sipp},j} \geq 1.99$  and (consequently) for non-synchronized to  $N_{\text{sipp},j} < 1.99$ .

## 2.5 Choice of system parameters

For our study, we adopt the nominal parameters from the tuned system configuration that was studied by Weidemann et al. [55]. In this case, the cyclic chain consists of  $N_s = 10$  sectors. In linear rotationally periodic structures, the largest resonant amplitude in the presence of mistuning is known to increase with the number of sectors  $N_s$  [66]. Therefore, we also expect the quantitative results on the localized vibration levels and localization intensities presented in this work to change when the number of sectors is varied, and emphasize that a quantitative mistuning analysis must always be performed for the specific system configuration at hand. Nevertheless, we believe that the chosen configuration with  $N_s = 10$  sectors is well suited to identify the potential interaction effects between Anderson localization and LSRs qualitatively, as well as to provide a quantitative estimate for systems with a similar number of sectors. The linear modal damping is assumed to be uniform with a modal damping ratio of  $D_l = 0.1\%$ . This weak modal damping is representative for realistic engineering structures in the absence of (other) mitigation devices [67]. We further consider a small mass ratio of  $\varepsilon_a = 2\%$  and treat impacts with a restitution coefficient of  $e_N = 0.8$ . Based on an analytical estimation of the GSR’s resonant amplitude in the tuned system, a nominal clearance of  $\Gamma = 0.33 \cdot \hat{q}_{\text{ref}}$  (cf. Eq. (18)) was identified as the VI-NESs’ optimal design point at which the highest resonant amplitude reduction is achieved for the aforementioned parameter values [55]. It should be noted that the existence of an “optimal clearance” is a direct consequence of the normalization adopted from [55] with a constant forcing amplitude (cf. Eq. (3)). An alternative means of introducing dimensionless variables would be to normalize the displacements by the size of the clearance. The latter would yield an optimal excitation level for the fixed clearance of unity. Therefore, one can easily see that a variation of the clearance for a

**Table 1** Values of the nominal system parameters

| $N_s$ | $D_l$ | $\varepsilon_a$ | $e_N$ | $\Gamma$                   | $\kappa_c$        |
|-------|-------|-----------------|-------|----------------------------|-------------------|
| 10    | 0.1 % | 2 %             | 0.8   | $0.33 \cdot \hat{q}_{ref}$ | $6 \cdot 10^{-3}$ |

fixed forcing amplitude has the same qualitative effect as the variation of the forcing amplitude for a fixed clearance. When compared to numerical simulations, it was shown that the aforementioned analytical estimation approximates the clearance’s actual optimal design point for the system’s non-localized solutions well [55], and its value will therefore be adopted herein. We note that the selected value of the clearance also seems to approximate the optimal design point of the mistuned system well in a statistical sense, which we tested for some representative examples of EM and CM in Appendix A. Lastly, as already shown for the tuned version of the system configuration considered herein [55], particularly large amplitudes of the LSR are found for weak inter-sector coupling strengths in the order of  $\kappa_c \sim 10^{-3}$ . Hence, a corresponding value of  $\kappa_c = 6 \cdot 10^{-3}$  is chosen throughout this work. We note that increasing the inter-sector coupling strength  $\kappa_c$  is known to diminish both Anderson and nonlinear localization. Hence, considering stronger coupling between the sectors is not expected to reveal stronger localization effects and is thus omitted in the present work. For a detailed study on the influence of the inter-sector coupling strength on the vibration level on LSRs in the tuned system, the reader is referred to [55]. All of the aforementioned parameter values are summarized in Table 1.

### 3 Analytical model of the locally synchronized responses (LSRs)

As a basis for our analysis on the interaction between mistuning and LSRs, we integrate EM and CM into the analytical single-term Harmonic Balance (HB, [68]) model of LSRs derived in [55]. This allows us to study the LSR’s parameter dependencies explicitly while also providing a computationally efficient yet accurate estimation of the frequency-amplitude curves and their stability. We note that the following derivation closely follows that of the tuned system’s LSRs shown in [55], with the only difference being the addition of the mistuning terms. Nevertheless, we decided to include the full derivation in the present work to clearly demonstrate how EM and CM enter into the model, and show that no additional assumptions (beyond those already introduced for the tuned system [55]) are required.

### 3.1 Single-term harmonic balance ansatz

LSRs are Chimera-like steady-state vibrations in which the motions of some VI-NESs and their respective host oscillators are synchronized in only a subset of sectors. For small mass ratios between the VI-NESs and their host oscillators, as considered herein (cf. Table 1), it was shown in [51], as well as in our previous study [55], that the steady-state motion of the host oscillators can be well-approximated as being harmonic. This allows us to express the displacements  $q$ , velocities  $u$ , and velocity measures  $du$  of the host oscillators in terms of a (single-term) truncated Fourier series:

$$\begin{aligned}
 q &\approx \text{Re} \left\{ \hat{Q} e^{ir\tau} \right\}, \quad u \approx \text{Re} \left\{ ir \hat{Q} e^{ir\tau} \right\}, \\
 du &\approx \text{Re} \left\{ -r^2 \hat{Q} e^{ir\tau} \right\} d\tau.
 \end{aligned}
 \tag{24}$$

Herein,  $Q \in \mathbb{C}^{N_s}$  is the vector of complex harmonic amplitudes of each oscillator,  $\hat{Q}_j$ , which can be further decomposed into a real amplitude  $\hat{q}_j = |\hat{Q}_j|$  and phase angle  $\gamma_j = \arg\{\hat{Q}_j\}$ , where  $\arg\{\square\}$  denotes the complex argument. To obtain the sought vector of complex harmonic amplitudes of the approximation,  $\hat{Q}$ , the well-known HB method [68] is applied as follows. The harmonic ansatz in Eq. (24) is inserted into the EOMs of all host oscillators in Eq. (9). This yields a residual vector, which is then required to vanish in average per oscillation period,  $T = 2\pi/r$ , weighted by the term  $e^{-ir\tau}$ . This is equivalent to requiring that the fundamental Fourier coefficient of the residual vector is zero. With this, one obtains a complex algebraic system of equations of the form:

$$\underbrace{\left[ -r^2 \mathbf{M} + ir \mathbf{C} + (\mathbf{K} + \delta \mathbf{K}) \right]}_{=:S(r)} \hat{Q} + \hat{\Pi}(\hat{Q}, r, S) = \hat{F}_{k_0}. \tag{25}$$

The HB method can be interpreted as a Fourier-Galerkin projection. We refer to the vector  $\hat{\Pi}$  as the vector of fundamental Fourier coefficients of the contact percussions  $\Pi$ . A derivation of its entries and a definition of the set  $S$  that  $\hat{\Pi}$  depends on are provided in the following.

### 3.2 Fourier coefficient of the contact percussions

When comparing the representative motion of a VI-NES in a synchronized and a non-synchronized sector in Fig. 1, it is evident that the corresponding Fourier coefficients of the resulting contact percussion require a different treatment in each of the two cases. This distinction is expressed in Eq. (25) by the dependence of  $\hat{\Pi}$  on the set  $S \subset \{1, \dots, N_s\}$ , in which we gather the indices of all synchronized sectors. For now,  $S$  is not further specified and it suffices to say that the analytical model may generally be used to analyze LSRs with different

permutations of synchronized and non-synchronized sectors, which theoretically also includes the special case of GSRs in which  $\mathcal{S} = \{1, \dots, N_s\}$  [55].

### 3.2.1 Synchronized sectors

In each synchronized sector,  $j \in \mathcal{S}$ , the VI-NES engages into a sustained 1:1 resonance capture with its host oscillator. Under the assumption of two symmetric impacts per period, the motion of the VI-NES,  $q_{a,j}$ , takes on the form of a triangle wave [47, 51]. The latter is schematically shown in Fig. 3 (red line) and can be expressed mathematically as:

$$q_{a,j} = \begin{cases} \frac{2\hat{q}_{a,j}}{\pi} \arcsin(\cos(r\tau + \gamma_j - \Delta_j)) & \text{if } j \in \mathcal{S} \\ 0 & \text{if } j \notin \mathcal{S} \end{cases} \quad (26)$$

Herein,  $\hat{q}_{a,j}$  is the real-valued amplitude of the triangle wave motion and  $\Delta_j$  describes the relative phase angle between the impact at the right cavity wall and the host oscillator's largest positive displacement (see Fig. 3). The case for the non-synchronized sectors,  $j \notin \mathcal{S}$ , in Eq. (26) will be discussed in Section 3.2.2. Given the assumptions for the motions of the host oscillator  $q_j$  and its VI-NES  $q_{a,j}$  in Eqs. (24) and (26), the Fourier coefficient of the contact percussion  $\hat{\Pi}_j$  can now be determined by reconstructing the impulsive contact reactions  $\Lambda_{N,j}^{L,R}$  from the impact law in Eqs. (6) and (7), and projecting them onto the harmonic motion. For a more detailed derivation of this step, the reader is referred to the study on the tuned system [55]. In the present work, however, we simply adopt the resulting expression for the fundamental Fourier coefficient of the contact percussions:

$$\hat{\Pi}_j = \begin{cases} -\frac{8\varepsilon_a \hat{q}_{a,j} r^2}{\pi^2} e^{i(\gamma_j - \Delta_j)} & \text{if } j \in \mathcal{S} \\ 0 & \text{if } j \notin \mathcal{S} \end{cases} \quad (27)$$

Herein, the triangle wave amplitude  $\hat{q}_{a,j}$  as well as the phase angle  $\Delta_j$  appear as independent variables. However, it was shown by Gendelman [47] that these are related to the harmonic amplitude of the host oscillator  $\hat{q}_j = |\hat{Q}_j|$  on a *slow invariant manifold* (SIM). The SIM consists of a coexisting stable and unstable branch. In this work, we are only interested in solutions on the stable branch of the SIM, which can be expressed as:

$$\hat{q}_{a,j} = \frac{\Gamma(1 + \delta_{\Gamma,j}) + \sqrt{(1 + \rho^2)\hat{q}_j^2 - (\rho\Gamma)^2(1 + \delta_{\Gamma,j})^2}}{1 + \rho^2}, \quad (28)$$

$$\hat{q}_j > \frac{\rho\Gamma(1 + \delta_{\Gamma,j})}{\sqrt{1 + \rho^2}}, \quad (28)$$

$$\Delta_j = \arccos\left(\frac{\hat{q}_{a,j} - \Gamma(1 + \delta_{\Gamma,j})}{\hat{q}_j}\right), \quad (29)$$

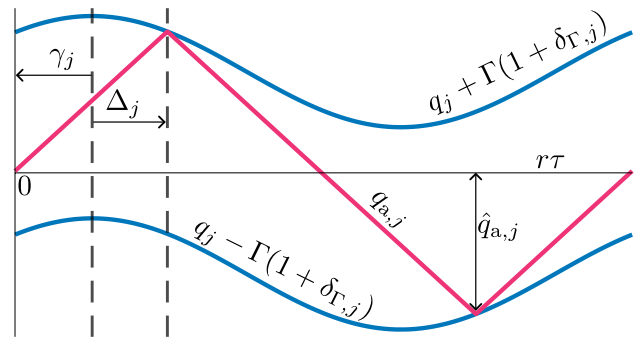


**Fig. 3** Definition of the amplitudes and phase angles in a synchronized sector. The blue lines indicate the motions of the cavity walls and the red line shows the triangle wave motion of the VI-NES. Illustration adopted from [55]

where  $\rho = \frac{2}{\pi} \frac{1 - \varepsilon_N}{1 + \varepsilon_N}$  is an auxiliary variable. With Eqs. (28) and (29), the Fourier coefficient for the synchronized sectors,  $j \in \mathcal{S}$ , in Eq. (27) can be explicitly parameterized in terms of the oscillator's amplitude  $\hat{q}_j = |\hat{Q}_j|$ . The condition on the size of the amplitude  $\hat{q}_j$  in Eq. (28) indicates a fold bifurcation, below which the SIM ceases to exist [47]. The physical interpretation of this fold bifurcation is that not enough energy is being supplied to the sector to maintain a sustained 1:1 resonance capture between the host oscillator and the VI-NES at lower amplitudes [51]. It should also be noted that the stable branch of the SIM was shown to lose its stability for amplitudes beyond  $\hat{q}_j \geq \frac{\Gamma(1 + \delta_{\Gamma,j})\sqrt{\pi^4 \rho^2 + 16}}{\pi^2 + 4}$  [69]. This stability loss gives rise to a large variety of impact sequences other than two symmetric impacts per period that arise in the case of a symmetric triangle wave motion [70]. In the present work, however, we neglect the SIM's stability loss at large amplitudes and also use the relations in Eqs. (28) and (29) beyond this upper amplitude bound. Nevertheless, we emphasize that, even beyond the stability loss, the resulting oscillator amplitude(s) of analytical models relying on the assumptions in Eqs. (24) and (26) have shown to agree well with those determined from numerical simulations, which have a variety of impact sequences (see e.g. [55, 71]).

### 3.2.2 Non-synchronized sectors

Strictly speaking, the Chimera-like character of the LSR with irregular and non-periodic impacts of the VI-NESs in the non-synchronized sectors is not amenable to our HB ansatz, which (per definition) requires periodicity. However, we already showed for the tuned system [55] that LSRs can be well approximated in an idealized form, when assuming that the VI-NESs do not come into contact with the cavity walls in all non-synchronized sectors,  $j \notin \mathcal{S}$ . This is achieved by placing them at rest at the center of their cavity, which yields the trivial solution for their motion,  $q_{a,j} = 0$  (see Eq. (26)). Clearly, if no impacts occur, the resulting Fourier

coefficients of the contact percussions,  $\hat{\Pi}_j$ , are also given by the trivial solution (see Eq. (27)). An alternative way of motivating a trivial solution for  $\hat{\Pi}_j$  in the non-synchronized sectors is to consider that the irregular impacts occur at “random” phases, relative to the motion of their host oscillators. Hence, the resulting contact reactions are expected to approximately average to zero when projected onto the fundamental harmonic. Independent of the interpretation, this simplification is only valid if the amplitudes of the host oscillators are smaller than the size of the clearance  $\Gamma(1 + \delta_{\Gamma,j})$  in *all* non-synchronized sectors, i. e.,  $\hat{q}_j < \Gamma(1 + \delta_{\Gamma,j}) \forall j \notin \mathcal{S}$ . We call this condition the *kinematic constraint* of the assumption, as the VI-NESs in sectors that violate this constraint would inevitably engage into either transient or sustained 1:1 resonance captures with their host oscillators. When motivating our assumption of a trivial Fourier coefficient from an “idealized LSR” with a trivial motion of the VI-NESs in the non-synchronized sectors, the kinematic constraint can also be viewed as a *grazing bifurcation* [72]. This is because the idealized state would cease to exist as the cavity walls begin to graze the VI-NES at  $q_{a,j} = 0$  if  $\hat{q}_j = \Gamma(1 + \delta_{\Gamma,j})$ .

### 3.2.3 Comment on additional coupling between the cavity and the VI-NES

In the present work, we assume that each VI-NES is solely coupled to its host oscillator via the unilateral constraints at the cavity walls. This modeling choice is reflected in the derivation of the fundamental Fourier coefficients  $\hat{\Pi}_j$  for both the synchronized and the non-synchronized sectors in Eq. (27). In real applications, however, effects like dry friction between the VI-NES and the cavity, or viscous forces due to a fluid-filled cavity, may introduce an additional coupling mechanism between each VI-NES and its host oscillator. Dry friction is known to neither significantly impede nor significantly improve the performance of a VI-NES (in the case of a non-periodic host structure; synchronized regime) [73]. Hence, the strongest influence of additional coupling mechanisms is expected to occur in the non-synchronized sectors, and on the way these are treated analytically when attempting to idealize the Chimera-like character of the LSR. If the additional coupling effects are strong, it may be more appropriate to assume that the VI-NESs are stuck to their host oscillators in all synchronized sectors,  $j \notin \mathcal{S}$ , rather than being at rest at  $q_{a,j} = 0$ . In this case, the masses of the sticking VI-NESs may simply be added to the corresponding diagonal entries of the system’s mass matrix,  $\mathbf{M}$ , on the left-hand side of Eq. (25). This can be interpreted as a deterministic form of (small) mass mistuning, which is expected to yield similar effects as those we will later report for EM (which is introduced through the grounding stiffness) in Section 4. In addition to the modeling of the idealized LSR, the previously introduced kinematic constraint would no longer apply in its

current form, and would need to be adjusted to the specific coupling mechanism at hand, e. g., a VI-NES can no longer stick after the maximum static friction force is exceeded. We note that this may allow for an LSR to exist across a much larger region of excitation frequencies and amplitudes than what is reported in both our present and previous studies [55]. In the practically relevant case of dry friction between the VI-NES and the cavity, however, we expect ball-shaped VI-NESs to start rolling rather than sliding or sticking [50]. This is expected to yield negligible added mass effects.

### 3.3 Stability analysis

To determine the local asymptotic stability of an LSR, we can exploit the fact that solutions for the complex amplitudes,  $\hat{Q}$ , of the HB system in Eq. (25) can be interpreted as fixed points of the *slow flow equations* derived with Manevitch’s complexification averaging (CX-A) technique [74]. Hence, the local asymptotic stability can be determined via linearization of the slow flow equations close to their fixed points, which is described in more detail in Appendix B. A limitation of this approach is that it is consequentially limited to the underlying idealization of the LSR in which no impacts occur in the non-synchronized sectors. However, in view of the Chimera-like character of “true” LSRs, which exhibit irregular impacts in the non-synchronized sectors, the practical meaning of local asymptotic stability alone is limited. In other words, local asymptotic stability can be understood as a necessary but not a sufficient property that an LSR needs to possess to be of “practical relevance”. To address the effect of impacts in the non-synchronized sectors on the LSR’s stability, we adopted the analysis for (what we herein define as) *practical stability* from [55], which is based on numerical time-step integration. To this end, we initialized the host oscillators of *all* sectors, and the VI-NESs in the *synchronized* sectors on the analytical solution according to Eqs. (24) and (26). In the *non-synchronized* sectors, however, we initially placed all VI-NESs close to the left cavity wall,  $q_{a,j}(0) = q_j(0) - \Gamma(1 + \delta_{\Gamma,j})$ , with zero relative velocities,  $u_{a,j}(0) = u_j(0)$ . This caused impacts in all non-synchronized sectors shortly after the simulation started. If an LSR is practically stable, the resulting motion of the VI-NESs in the non-synchronized sectors simply becomes irregular, as shown in the representative example at the bottom of Fig. 1, while the synchronized sectors remain synchronized. If an LSR is practically unstable, however, the impacts in the non-synchronized sectors either cause some initially non-synchronized sectors to become synchronized, or cause some initially synchronized sector to lose their synchronization. We tested these qualitative criteria by simulating for 1300 excitation periods and counting the average number of significant impacts per period in each sector,  $N_{\text{sipp},j}$ , over the last

300 excitation periods of each simulation (cf. Section 2.4). An LSR was deemed practically stable if

1. the initially synchronized sector remains synchronized, i. e.,  $N_{\text{sipp},j} \geq 1.99 \forall j \in \mathcal{S}$ , and
2. all initially non-synchronized sectors remain non-synchronized, i. e.,  $N_{\text{sipp},j} < 1.99 \forall j \notin \mathcal{S}$ ,

and practically unstable if at least one of the above criteria was not fulfilled. Increasing the simulation time for the practical stability analysis procedure was found not to alter the results presented herein. It should be emphasized that we focus on practical stability as our primary stability measure and only utilize the local asymptotic stability analysis to identify potential solutions that could be practically stable [55]. Lastly, we note that additional coupling mechanisms between the VI-NESs and their host oscillators (e.g. dry or viscous friction), as discussed in Section 3.2.3, can potentially prevent impacts in the non-synchronized sectors, or at least diminish their intensity. In that case, no strong difference between local asymptotic and (our definition of) practical stability is expected.

### 3.4 Condensation to a single synchronized sector

In our previous study on the tuned system [55], we showed that the system's steady-state dynamics can settle to many different LSRs, each with a unique permutation of synchronized and non-synchronized sectors, i. e., a different set  $\mathcal{S}$ , depending on the initial conditions. Hence, for a given tuned or mistuned realization of the system, many LSRs with different sets  $\mathcal{S}$  may possibly coexist. An attempt to estimate how many LSRs may possibly coexist in a given mistuned realization of the system is provided in Appendix C. To show that the analytical model can be used to analyze LSRs with arbitrary permutations of synchronized and non-synchronized sectors, we did not specify a particular set of synchronized sectors  $\mathcal{S}$  thus far. However, we note that a detailed analysis of all possible LSRs, i. e., LSRs with all possible sets  $\mathcal{S}$ , would be infeasible, even if only a single mistuned realization of the system would be considered. For this reason, we will focus on the extreme case of a single synchronized sector instead. In the tuned system, this has been shown to lead to strong nonlinear localization and provided close approximations of the maximally-achievable nonlinearly-localized amplitude when compared to other LSRs with multiple synchronized sectors [55]. We assume that this applies to the mistuned system as well, and leave an investigation of finding the permutation of synchronized and non-synchronized sectors that yields the highest amplitudes for future work. In the case of a single synchronized sector, the set  $\mathcal{S}$  becomes a singleton  $\mathcal{S} = \{s\}$ , where  $s \in \{1, \dots, N_s\}$  is the index of the synchronized sector. If the system is tuned and therefore

possesses ideal cyclic symmetry, the corresponding LSRs' behavior, in terms of their amplitudes and stability, is identical for all possible (single) synchronized sectors  $s$  [55]. In each mistuned realization of the system, however, the cyclic symmetry is broken, and the LSRs' behavior must generally be expected to depend on the specific synchronized sector  $s$ . Hence, the index of the synchronized sector  $s$  is not further specified in the following derivation.

At this point it should be recalled that we assumed a trivial Fourier coefficient of the contact percussions for all non-synchronized sectors, i. e.,  $\hat{\Pi}_{j \neq s} = 0$  (cf. Eq. (27)). This means that the complex algebraic system of equations in Eq. (25), which governs the unknown amplitudes of the host oscillators,  $\hat{\mathbf{Q}}$ , is only nonlinear in terms of the amplitude of the synchronized sector  $\hat{Q}_s$ . The unknown amplitudes of the non-synchronized sectors  $\hat{Q}_{j \neq s}$  are simply linearly coupled to  $\hat{Q}_s$  via the dynamic stiffness matrix  $\mathbf{S}$  (see definition in Eq. (25)). Hence, by left-multiplying Eq. (25) with the dynamic compliance matrix  $\mathbf{H} = \mathbf{S}^{-1}$ , we obtain a decoupled, scalar complex algebraic equation that only depends on the amplitude of the synchronized sector  $\hat{Q}_s$ . This step is analytically exact and known as the Condensation Method [68]. The resulting decoupled equation is read as:

$$\hat{q}_s e^{i\gamma_s} - H_{ss} \frac{8\varepsilon_a \hat{q}_{a,s} r^2}{\pi^2} e^{i(\gamma_s - \Delta_s)} = \hat{Q}_s^{\text{lin}}. \quad (30)$$

Herein, the complex amplitude  $\hat{Q}_s$  was additionally decomposed into its real amplitude  $\hat{q}_s$  and complex phase  $\gamma_s$  by using the relation  $\hat{Q}_s = \hat{q}_s e^{i\gamma_s}$ . Moreover,  $H_{ss}$  refers to the  $s$ -th diagonal entry of the dynamic compliance matrix,  $\mathbf{H}$ , and  $\hat{Q}_s^{\text{lin}}$  is the complex amplitude of the respective oscillator in the linear case with removed VI-NESs (mass deficiency). The latter is given by the  $s$ -th entry of the vector of linear complex amplitudes of all oscillators  $\hat{\mathbf{Q}}^{\text{lin}} = \mathbf{H} \hat{\mathbf{F}}_{k_0}$ . Recall that the VI-NES's triangle wave amplitude  $\hat{q}_{a,s}$ , and the phase shift  $\Delta_s$  in Eq. (30) explicitly depend on the real amplitude of the synchronized sector  $\hat{q}_s$  through Eqs. (28) and (29). While Eq. (30) could already be solved numerically for  $\hat{q}_s$  and  $\gamma_s$ , we proceed to follow the approach presented in [55] of deriving a *Frequency Response Surface* (FRS) for the LSR. We believe that this enables a better interpretation of the parameter dependencies. We introduce our definition of the FRS in the following Section 3.5.

### 3.5 Frequency response surface

In order to derive the FRS, we first introduce the real, clearance-normalized oscillator and VI-NES amplitudes,  $\xi$  and  $\vartheta$ , as:

$$\xi = \frac{\hat{q}_s}{\Gamma(1 + \delta_{\Gamma,s})}, \quad \vartheta = \frac{\hat{q}_{a,s}}{\Gamma(1 + \delta_{\Gamma,s})}. \quad (31)$$

When substituting these new variables into the condensed Eq. (30), we can factor out the clearance  $\Gamma(1 + \delta_{\Gamma,s})$  on the left-hand side and divide both sides by the remaining term. After further taking the absolute value to eliminate the complex phase shift  $e^{i\gamma_s}$ , Eq. (30) can be reformulated to:

$$\Gamma(1 + \delta_{\Gamma,s}) = \left| \frac{\hat{Q}_s^{\text{lin}}}{\xi_s - H_{ss} \frac{8\varepsilon_a \vartheta r^2}{\pi^2} e^{-i\Delta_s}} \right|. \tag{32}$$

Thereby, the clearance-normalized VI-NES amplitude  $\vartheta$  and the phase angle  $\Delta_s$  only depend on  $\xi$ . This can be shown by substituting the clearance-normalized amplitudes,  $\xi$  and  $\vartheta$ , into the expression of the stable branch of the SIM in Eqs. (28) and (29), which eliminates the dependence on the clearance  $\Gamma(1 + \delta_{\Gamma,s})$ :

$$\vartheta = \frac{1 + \sqrt{(1 + \rho^2)\xi^2 - \rho^2}}{1 + \rho^2}, \quad \xi > \frac{\rho}{\sqrt{1 + \rho^2}}, \tag{33}$$

$$\Delta_s = \arccos\left(\frac{\vartheta - 1}{\xi}\right). \tag{34}$$

Recall that  $\rho = \frac{2}{\pi} \frac{1-\varepsilon_N}{1+\varepsilon_N}$  is a constant auxiliary variable. We call the expression in Eq. (32) the FRS of the LSR with a single synchronized sector, as it maps each combination of the clearance-normalized amplitude  $\xi$  and the excitation frequency  $r$  to a unique value of the clearance  $\Gamma(1 + \delta_{\Gamma,s})$ . This means that the level-curves of Eq. (32), for  $\Gamma(1 + \delta_{\Gamma,s}) = \text{const.}$ , determine the curves of constant system parameters but varying amplitude and excitation frequency, i.e., they directly govern the frequency-amplitude curves<sup>1</sup>. At this point, one can already see an important difference between EM and CM. Since EM is introduced via the stiffness mistuning matrix  $\delta\mathbf{K}$ , it directly influences the host structure’s dynamic compliance matrix  $\mathbf{H} = \mathbf{S}^{-1}$  (cf. Eq. (25)) and, thus, the diagonal entry  $H_{ss}$  and the linear complex amplitude  $\hat{Q}_s^{\text{lin}}$  on the right-hand side of Eq. (32). This means that EM directly alters the shape of the FRS. CM, on the other hand, only changes the value of the clearance on the left-hand side of Eq. (32) at which the level curve,  $\Gamma(1 + \delta_{\Gamma,s}) = \text{const.}$ , that governs where the frequency-amplitude curve is evaluated. We also note that the kinematic constraint, as introduced in Section 3.2.2, cannot be directly enforced in the expression of the FRS in Eq. (32). Hence, solutions on the FRS that violate the kinematic constraint must be filtered out *a posteriori*. To this end, the amplitudes of the non-synchronized sectors,  $\hat{Q}_{j \neq s}$ , must be computed in a subsequent expansion.

<sup>1</sup> We determine the level curves by sampling the FRS on a finely resolved grid spanned by  $\xi$  and  $r$ , and interpolating the level curve between these points. We found that this approach is computationally cheap and delivers accurate results if the grid is fine enough.

### 3.6 Expansion of the non-synchronized sectors

Along the level curves of the FRS in Eq. (32), the amplitude of the synchronized sector’s oscillator is given in terms of its clearance-normalized value  $\xi$ . To obtain the complex amplitudes of all (synchronized and non-synchronized) sectors,  $\hat{Q}_j$ , we first compute the clearance-normalized amplitude of the VI-NES,  $\vartheta$ , and the phase angle  $\Delta_s$  for every known value of  $\xi$  by using Eqs. (33) and (34). Since the clearance  $\Gamma(1 + \delta_{\Gamma,s})$  is also known and constant along the level curve, the real amplitudes of the synchronized sector’s oscillator,  $\hat{q}_s$ , and its VI-NES,  $\hat{q}_{a,s}$ , can be obtained by un-normalizing  $\xi$  and  $\vartheta$  according to Eq. (31). Further, it suffices to implicitly compute the complex phase  $\gamma_s$  in its exponential form  $e^{i\gamma_s}$  by factoring out the latter on the left-hand side of Eq. (30) and dividing by the remaining expression:

$$e^{i\gamma_s} = \frac{\hat{Q}_s^{\text{lin}}}{\hat{q}_s - H_{ss} \frac{8\varepsilon_a \hat{q}_{a,s} r^2}{\pi^2} e^{-i\Delta_s}}. \tag{35}$$

Lastly, we use the remaining decoupled equations from the condensation step, i.e., the left-multiplication of Eq. (25) with the dynamic compliance matrix  $\mathbf{H} = \mathbf{S}^{-1}$ , to determine all complex amplitudes  $\hat{Q}_j$  based on the known quantities:

$$\hat{Q}_j = \hat{Q}_j^{\text{lin}} + H_{js} \frac{8\varepsilon_a \hat{q}_{a,s} r^2}{\pi^2} e^{i(\gamma_s - \Delta_s)}, \quad j = 1, \dots, N_s. \tag{36}$$

Herein,  $H_{js}$  is the scalar partition of the dynamic compliance matrix  $\mathbf{H}$  that governs the dynamic compliance of sector  $j$  to a harmonic force acting on the synchronized sector  $s$ . Note that Eq. (36) also applies to the amplitude of the synchronized sector  $\hat{Q}_s$ .

## 4 Eigenfrequency mistuning

We first consider the case of EM and assume all clearances to be perfectly tuned, i.e.,  $\delta_{\Gamma} = \mathbf{0}$ . Since EM alters the shape of the FRS itself, as discussed in Section 3.5, we first study its influence on the FRS based on a representative realization of the mistuning pattern,  $\delta_r$ , in Section 4.1. A statistical analysis with a focus on practically stable solutions is then provided in Section 4.2.

### 4.1 Influence on the FRS

The FRS of the tuned system, in the case of excitation wavenumber  $k_0 = 1$ , is shown at the top in Fig. 4, where the solid black lines depict representative level curves for different clearances  $\Gamma$ , i.e., frequency-amplitude curves in terms of the clearance-normalized amplitude  $\xi$ . As already reported in [55], the FRS possesses multiple local maxima

that each host isolated frequency-amplitude curves (open or closed depending on the value of the clearance  $\Gamma$ ) with corresponding resonances. Throughout the rest of this work, we use the terms *resonance* to refer to a local amplitude maximum of the frequency-amplitude curves and *resonance frequency* to refer to the respective excitation frequency  $r$ . The value of the clearance  $\Gamma$  at a local maximum of the FRS indicates a fold bifurcation of the corresponding isolated frequency-amplitude curve that contracts to a single point and ultimately ceases to exist as the clearance  $\Gamma$  is further increased. For a more detailed discussion on the behavior of the FRS in the tuned system, the interested reader is referred to [55].

We now aim to analyze how EM alters the FRS qualitatively and how these changes evolve as the mistuning level  $\sigma_r$  is varied. To this end, we generated a representative realization of a mistuning pattern  $\delta_r^*$ , shown in Table 3 in Appendix D, with a spatial mistuning intensity of unity. More specifically,  $\delta_r^*$  is normalized to possess a corrected sample standard deviation, taken over all sectors, of 1. The actual mistuning pattern  $\delta_r$ , that is introduced to the system can now be defined as  $\delta_r = \sigma_r \delta_r^*$ . We emphasize that we only momentarily adjust the spatial mistuning intensity in a deterministic manner as a means of investigating the effect of the mistuning level without changing the mistuning pattern  $\delta_r^*$  qualitatively. The synchronized sector is set to  $s = 1$ . As EM is introduced to the system, the shape of the FRS changes drastically. For the smallest mistuning level of  $\sigma_r = 1\%$ , depicted in Fig. 4, the isolated frequency-amplitude curves are strongly distorted compared to the tuned case. Moreover, the values of the clearance  $\Gamma$  at the local maxima is strongly affected, meaning that the LSR might exist over a wider (or smaller) range of clearances  $\Gamma$  than what is predicted by the FRS of the tuned system. When the mistuning level  $\sigma_r$  increases, new local maxima/isolated frequency-amplitude curves emerge in the vicinity of the existing local maxima (see  $\sigma_r = 2\%$  in Fig. 4). These new branches then start to detach and become well-separated from one another as the mistuning level is further increased (see  $\sigma_r = 4\%$  in Fig. 4). It thus appears that increasing the mistuning level  $\sigma_r$  has a similar qualitative effect as increasing the inter-sector coupling strength in the tuned system [55]. There, it was also observed that the FRS's local maxima split up and separate as the system's linear eigenfrequencies separate (cf. Eq. (13)), until the FRS possesses as many local maxima as linear eigenfrequencies (approximately  $N_s/2$  in the tuned system). Due to *mode splitting*, i. e., the loss of degeneracy of the pairs of traveling wave modes with the same absolute wavenumber  $|l|$  [6], the number of distinct linear eigenfrequencies in the system with EM, and thus the number of local maxima of the FRS, is equal to the number of sectors  $N_s$ . An important implication of these strong interaction effects is that the existence or non-existence of an LSR in a certain parameter range of the tuned

system does *not* imply the existence or non-existence of an LSR in the same (nominal) parameter range of a mistuned realization of the system. It should be emphasized that this statement also holds for the relation between two different mistuned realizations of the system. Even though the LSRs always appear in the frequency region close to  $r = 1$ , it is practically impossible to predict the exact frequency range at which the LSR exists, unless the specific mistuning pattern  $\delta_r$  is known.

## 4.2 Influence on practical stability

To address the influence of EM on the LSRs' practical stability, i. e., the property of an LSR to survive occasional impacts in the non-synchronized sectors (cf. Section 3.3), we now generate multiple realizations of mistuning patterns,  $\delta_r$ , via Monte-Carlo Simulations (MCSs). The number of MCSs is denoted by  $N_{\text{MCS}}$ . Note that the mistuning patterns are taken directly as described in Section 2.3.2 and are *not* additionally adjusted to exhibit a certain spatial standard deviation as in the previous Section 4.1. As already discussed during the derivation of the analytical model, each specific synchronized sector  $s \in \{1, \dots, N_s\}$  results in a unique qualitative and quantitative behavior of its corresponding LRSs. Moreover, LSRs with different single synchronized sectors  $s$ , may coexist in a given mistuned realization of the system (cf. Section 3.4). From a vibration mitigation perspective, however, the most relevant case for the single synchronized sector  $s$  is the one that that results in the largest practically stable amplitude, i. e.,  $\max_{s,r} \{\hat{q}_{\text{max}}\}$ . To find this "worst case synchronized sector"  $s$  for each mistuning pattern,  $\delta_r$ , we first extract the frequency-amplitude curves of the LSRs of all possible synchronized sectors  $s \in \{1, \dots, N_s\}$  from their FRSs, and analyze their practical stability. Throughout the rest of this work, we only present results on the LSRs with the synchronized sector  $s$  that yields the largest practically stable amplitude,  $\max_{s,r} \{\hat{q}_{\text{max}}\}$ . In our previous paper on the tuned system [55], we further showed that practically stable LSRs only exist in the frequency range below the *lowest possible resonance frequency* of the LSRs [55]. The latter refers to the resonance frequency of the frequency-amplitude curve that is formed by the lowest-frequency local maximum of the FRS. Consequently, if the clearance of the synchronized sector is larger than this local maximum, no practically stable LSRs are expected. As demonstrated in Appendix E, this also appears to apply in the presence of EM and, hence, we exclusively analyze this frequency region in the following analysis. Thereby, we focus on excitation wavenumbers  $k_0 = 0$ ,  $k_0 = 2$ , and  $k_0 = 5$  as representative cases in which:

- the tuned system exhibits practically stable LSRs ( $k_0 = 0$ ),

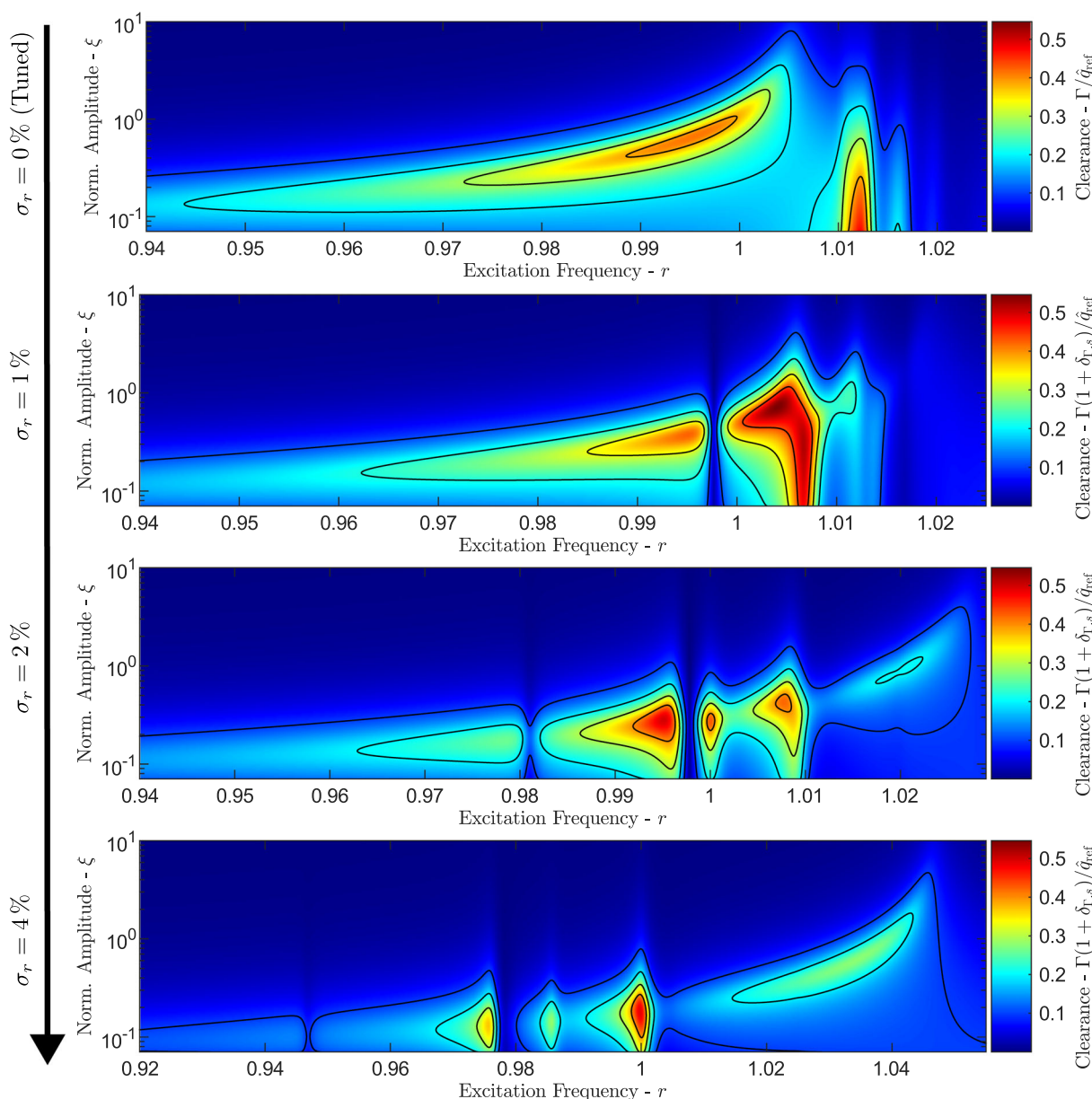


**Fig. 4** Representative evolution of the frequency response surface (FRS) for a locally synchronized response with fixed synchronized sector  $s$  and qualitative mistuning pattern  $\delta_r^*$ , but varying mistuning levels

$\sigma_r$ . The frequency axes for the two highest mistuning levels was adjusted compared to the lowest mistuning levels

- the LSRs’ frequency-amplitude curve around their lowest possible resonance frequency exists in the tuned system, but does not exhibit any practically stable solutions ( $k_0 = 2$ ), and
- the LSRs’ frequency-amplitude curve around their lowest possible resonance frequency does not exist in the tuned system ( $k_0 = 5$ ).

We begin by identifying how EM may qualitatively interact with practically stable LSRs, and then analyze the depen-

dence of the identified interaction effects on the mistuning level  $\sigma_r$ .

#### 4.2.1 Qualitative analysis

For our qualitative analysis on the possible interactions between LSRs and practically stable LSRs, we momentarily fix the mistuning level at  $\sigma_r = 1\%$ . Since EM strongly alters the shape of the FRS, it also drastically affects where the lowest possible resonance frequency of the LSR is found. This is

clearly visible for the case of a standing wave excitation with wavenumber  $k_0 = 0$ , for which the numerically determined practically stable amplitudes  $\hat{q}_{\max}$  based on  $N_{\text{MCS}} = 1000$  MCSs are shown by the gray point cloud in Fig. 5a. Each marker depicts the numerically determined amplitude during the last 300 excitation periods of the simulation performed in the practical stability analysis (see Section 3.3), while the color scale from white to black indicates an increasing LF (cf. Eq. (23)). For reference, the solid and dashed-dotted orange lines in the background indicate the linear frequency-amplitude curves of the tuned system with fixed or removed VI-NESs, respectively. Moreover, the blue line indicates the maximum amplitude  $\hat{q}_{\max}$  of the tuned system’s LSR, which coincides with the amplitude of its synchronized sector, i. e.,  $\hat{q}_{\max} = \hat{q}_s$ , in all examples in Fig. 5. Regions, in which the blue line is replaced by a red-dotted line, violate the kinematic constraint and, hence, are regarded as non-physical/non-realizable. The stability of the solutions in the tuned system is indicated by the respective markers: practically stable solutions are indicated by green stars, locally asymptotically stable but practically unstable solutions are indicated by blue dots, and unstable solutions are indicated by red dots. For additional stability analyses of entire frequency-amplitude curves in the mistuned system, the reader is referred to Appendix F. Interestingly, the depicted highest-amplitude LSRs mostly appear at excitation frequencies  $r$  lower than for the LSR in the tuned system. Thereby, one can observe a correlation between how far the frequency-amplitude curve is shifted to lower excitation frequencies  $r$ , and how high the resulting largest practically stable amplitudes  $\hat{q}_{\max}$  and LFs become. We note that the frequency-amplitude curves can generally also shift to higher frequencies when considering LSRs with other single synchronized sectors  $s$  that exhibit lower maximum practically stable amplitudes.

In addition to affecting the location of the frequency-amplitude curves, EM can also have a stabilizing effect. At this point, it should be recalled that the tuned system does not exhibit practically stable LSRs for excitation wavenumbers  $k_0 = 2$  and  $k_0 = 5$  in the considered configuration of nominal parameters [55]. When introducing EM, however, we could always find at least one synchronized sector,  $s \in \{1, \dots, N_s\}$ , that yields practically stable LSRs for excitation wavenumber  $k_0 = 2$ , as shown in Fig. 5b. Moreover, in 3.9% of the conducted MCSs at excitation wavenumber  $k_0 = 5$ , EM was capable of pushing the lowest-frequency local maximum of the FRS past the considered size of the clearance  $\Gamma$ , and even allowed for practically stable solutions on these newly-created frequency-amplitude curves (see Fig. 5c). It should be noted that the number of MCSs had to be increased to  $N_{\text{MCS}} = 5000$  to obtain sufficiently converged results for excitation wavenumber  $k_0 = 5$ . These findings further emphasize that one cannot rely on a qualitative assessment of whether practically stable LSRs exist

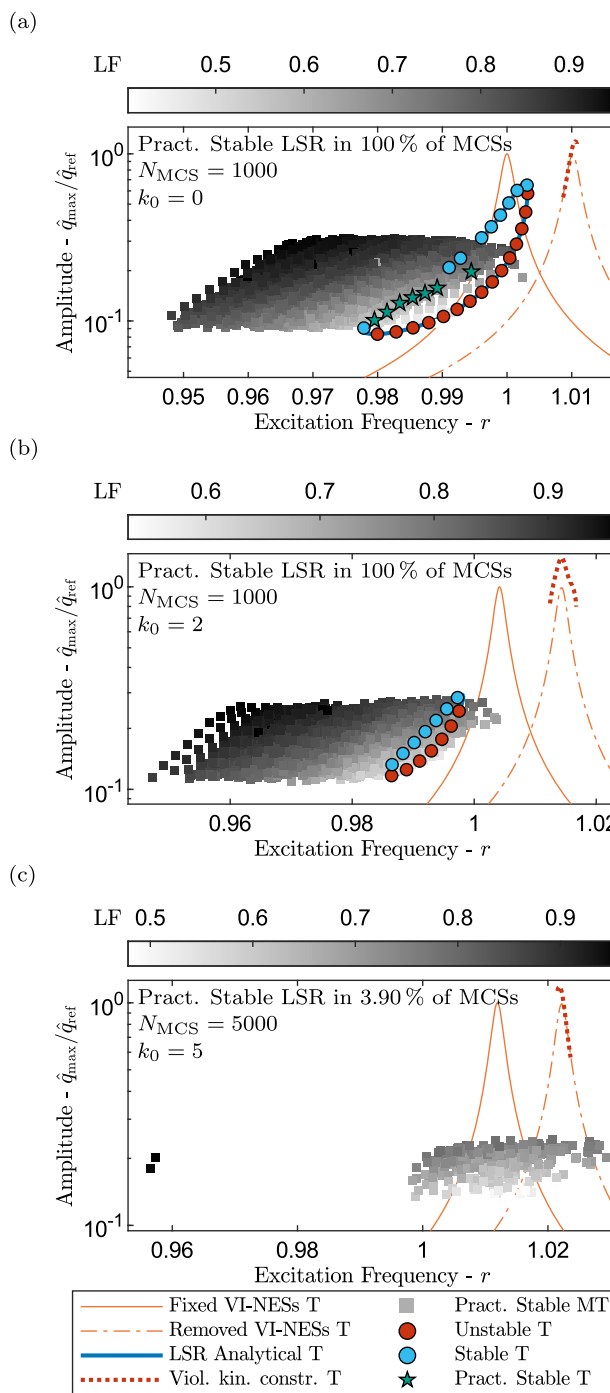


**Fig. 5** Locally synchronized response (LSR) with a single synchronized sector for the tuned (T) and mistuned (MT) system under EM for the fixed mistuning level of  $\sigma_r = 1\%$  and excitation wavenumbers (a)  $k_0 = 0$ , (b)  $k_0 = 2$ , and (c)  $k_0 = 5$

or not, that is solely based on the tuned system, even if the nominal parameter values are the same. The strong constructive interactions between EM and LSRs can be explained when considering that EM already leads to an intrinsic localization of the host structure’s linear modes. This means that the degree of localization of an LSR does not solely rely on

the locally acting, strong impact nonlinearity in the synchronized sector  $s$ , as it otherwise would in the tuned system. As pointed out in previous works [24–26], the well-known amplitude/energy-dependence of eigenfrequencies of nonlinear systems introduces an *effective mistuning* in nonlinear cyclic systems (even in the absence of structural mistuning), if the latter’s sectors oscillate at vastly different amplitudes. The effective mistuning of the system considered in the present work is a superposition of the random structural mistuning of the sectors’ local eigenfrequencies,  $\delta_r$ , and the effective change of the synchronized sector’s local eigenfrequency due to the locally acting impact nonlinearity; this superposition is always stronger than the effective mistuning of LSRs in the tuned system. Recall that we use the term “local eigenfrequency” to refer to the eigenfrequency of an isolated (uncoupled) sector. In summary, the presented results suggest that EM can create and/or practically stabilize LSRs, while also increasing the largest practically stable amplitudes and localization intensities (as quantified by the LF). The dependence of these interaction effects on the mistuning level  $\sigma_r$  is analyzed in the following.

#### 4.2.2 Influence of the mistuning level on the stabilization of LSRs

To quantify how likely it is that EM creates and/or practically stabilizes LSRs, we estimated the probability that practically stable LSRs exist for a given mistuning level  $\sigma_r$ . To this end, we counted the number of random realizations of mistuning patterns  $\delta_r$  for which we found practically stable LSRs in at least one synchronized sector  $s \in \{1, \dots, N_s\}$  and divided it by the total number of MCSs,  $N_{MCS}$ . The dependence of this probability on the mistuning level is shown in Fig. 6. In the case of excitation wavenumber  $k_0 = 0$ , where the tuned system already exhibits practically stable LSRs, the probability remains at 100 % for all considered mistuning levels  $\sigma_r$ . This means that EM did not lead to a destructive interaction with LSRs. Instead, the stabilizing effect of EM only increases as the mistuning level  $\sigma_r$  grows, which is shown by the increasing probability for excitation wavenumbers  $k_0 = 2$  and  $k_0 = 5$ . For both of these excitation wavenumbers,  $k_0$ , the probability that practically stable LSRs exists reaches nearly 100 % for the strongest considered mistuning level of  $\sigma_r = 4\%$ . This increase of the probability occurs faster, i.e., already for smaller mistuning levels  $\sigma_r$ , for excitation wavenumber  $k_0 = 2$  than for  $k_0 = 5$ . This is because the latter requires EM to not only alter the shape of the FRS strong enough to create a frequency-amplitude curve for the given clearance of  $\Gamma = 0.33 \cdot \hat{q}_{ref}$  but to also practically stabilize the LSRs. For excitation wavenumber  $k_0 = 2$ , on the other hand, only a practical stabilization of an already existing frequency amplitude curve is required. It should be emphasized that the probabilities shown in Fig. 6 do not dif-

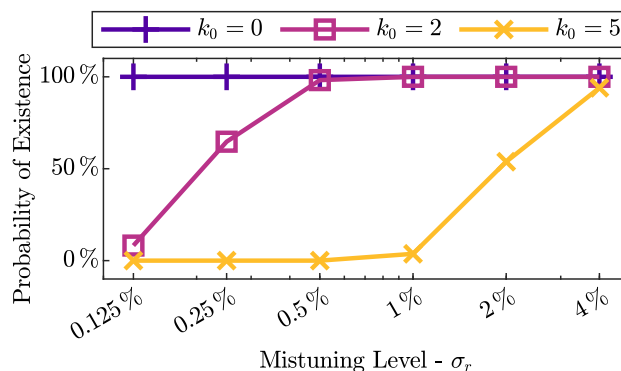
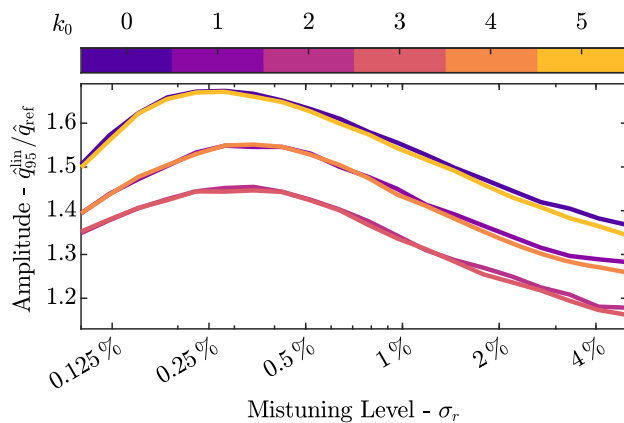


Fig. 6 Probability that a practically stable LSR exists for at least one single synchronized sector  $s \in \{1, \dots, N_s\}$ , depending on the EM mistuning level  $\sigma_r$

ferentiate between the creation of new frequency-amplitude curves or the stabilization of already existing LSRs. In view of the results presented above it may appear beneficial to choose much larger nominal clearances  $\Gamma$  than considered in the present work. This is because one would avoid practically stable LSRs entirely, even for the lowest excitation wavenumbers  $k_0$ , if the clearance is larger than the local maximum of the FRS that forms the frequency-amplitude curves around the lowest possible resonance frequency (which are known to host practically stable LSRs). However, this would also mean that the nominal clearance may be significantly larger than at its optimal design point (as chosen in the present work; see Appendix A). An interesting direction for future work would be to analyze whether this trade-off would be beneficial for the resulting vibration levels that may then be dominated by solutions without intrinsic nonlinear localization, i.e., GSRs or SMRs, or other LSRs with multiple synchronized sectors.

#### 4.2.3 Influence of the mistuning level on the maximum amplitudes

In view of the strong stabilizing effect of EM on LSRs, the imminent question arises of *how high the LSRs’ amplitudes become*. However, before addressing this directly, we first briefly discuss the well-studied influence of the mistuning level  $\sigma_r$  on the resonant amplitudes in the linear system with fixed VI-NESs (no mass deficiency). This aims to serve as a reference for the results presented on LSRs. As a scalar statistical measure of the linear resonant amplitudes, we determined their empirical 95 %-quantiles, denoted by  $\hat{q}_{95}^{lin}$ , for various mistuning levels  $\sigma_r$ , based on  $N_{MCS} = 10000$  MCSs each. The results are shown in Fig. 7, where each color indicates a different excitation wavenumber  $k_0$ . All depicted curves follow the same trend reported throughout the literature [9, 10, 13], namely that  $\hat{q}_{95}^{lin}$  increases with the mistuning level  $\sigma_r$  until it reaches a maximum and then decreases again. Depending on the excitation wavenumber  $k_0$ , the highest



**Fig. 7** Empirical 95 %-quantiles of the largest linear resonant amplitude,  $\hat{q}_{95}^{\text{lin}}$ , depending on the EM mistuning level  $\sigma_r$

**Table 2** Largest practically stable amplitude and LF of the LSR with a single synchronized sector in the tuned system for the nominal parameters in Table 1. For excitation wavenumbers  $k_0 \geq 2$ , no practically stable LSRs exist

|           | $\max_r \{\hat{q}_{\text{max}}\} / \hat{q}_{\text{ref}}$ | $\max_r \{\text{LF}\}$ |
|-----------|--|------------------------|
| $k_0 = 0$ | 0.197  | 0.708                  |
| $k_0 = 1$ | 0.131  | 0.617                  |

amplitudes  $\hat{q}_{95}^{\text{lin}}$  are reached for mistuning levels between  $0.2\% \leq \sigma_r \leq 0.4\%$ .

In the case of LSRs, we determined the largest amplitude that is reached for a random realization of the mistuning pattern  $\delta_r$  as the largest practically stable amplitude over all excitation frequencies  $r$  and synchronized sectors  $s$ , i. e.,  $\max_{r,s} \{\hat{q}_{\text{max}}\}$ . We gathered the largest practically stable amplitudes, and their corresponding LFs of the LSRs in the tuned system in Table 2. Different to the mistuned resonant amplitudes of the linear system  $\hat{q}_{95}^{\text{lin}}$  shown in Fig. 7, the highest practically stable amplitudes of LSRs, only increase and no maximum is reached within the considered range of mistuning levels  $\sigma_r$ . This is shown by the shaded regions in Fig. 8a, c, and e, which indicate the range in which the largest practically stable amplitude was within 90 % of all MCSs where a practically stable LSR was found, for excitation wavenumbers  $k_0 = 0$ ,  $k_0 = 2$ , and  $k_0 = 5$ , respectively. The regions are bounded by the empirical 5 %-quantiles (lower dashed lines) and 95 %-quantiles (upper dashed lines) of the largest practically stable amplitude. These bounds indicate amplitudes that are either likely to be exceeded (5 %-quantile) or likely not to be exceeded (95 %-quantile). As an additional measure of the likely or “average” largest practically stable amplitude, its empirical 50 %-quantile/median is depicted by the solid lines. For excitation wavenumber  $k_0 = 0$ , the largest practically stable amplitudes are always likely to be higher than in the tuned system (cf. Table 2 and hor-

izontal black line in Fig. 8a). The latter always remains below the empirical 5 %-quantile, and is thus likely to be exceeded, even for the smallest considered mistuning level of  $\sigma_r = 0.125\%$ . At the upper limit of mistuning levels,  $\sigma_r = 4\%$ , the largest practically stable amplitude of the mistuned system’s LSRs actually exceeded its corresponding value from the tuned case by a factor between 1.3 and 1.9 in 90 % of all MCSs. We note that we did not consider mistuning levels stronger than  $\sigma_r > 4\%$  as these would largely exceed realistic mistuning levels in engineering structures [75–77]. Moreover, we believe that these mistuning levels would be too high to still be viewed as mistuning in the sense of “perturbations” to the symmetry of the tuned system<sup>2</sup>. The largest practically stable amplitudes for excitation wavenumbers  $k_0 = 2$  and  $k_0 = 5$  in Fig. 8c and e exhibit the same qualitative dependence on the mistuning level  $\sigma_r$  as for  $k_0 = 0$ . However, the likely ranges of practically stable amplitudes at the same mistuning levels  $\sigma_r$  become lower as the excitation wavenumber  $k_0$  increases. Nevertheless, if the mistuning level  $\sigma_r$  is high, the largest practically stable amplitudes for  $k_0 = 2$  and  $k_0 = 5$  may still be larger than those observed in the tuned system at the lowest excitation wavenumbers  $k_0 = 0$  and  $k_0 = 1$ . We note that the amplitude ranges and quantiles for excitation wavenumber  $k_0 = 5$  in Fig. 8e are only shown for mistuning levels  $\sigma_r \geq 1\%$  since we did not observe practically stable LSRs for weaker mistuning, as already indicated by the zero probability in Fig. 6. Even though EM can significantly increase the maximum-achievable practically stable amplitudes compared to the tuned system’s LSRs, it should be emphasized that they always remain substantially lower than the linear resonant amplitude of the tuned system,  $\hat{q}_{\text{ref}}$  (fixed VI-NESs in all sectors). The latter serves as a normalizing constant for all amplitudes depicted in Fig. 8a, c, and e. This strong amplitude reduction effect is even more pronounced, when comparing the largest vibration levels of the LSRs in Fig. 8a, c, and e, to the empirical 95 %-quantile of the mistuned system’s linear resonant amplitudes,  $\hat{q}_{95}^{\text{lin}}$  in Fig. 7, which are even higher than in the tuned case. More specifically, while the linear mistuned resonant amplitudes  $\hat{q}_{95}^{\text{lin}}$  can grow between 40 %-60 % higher than the resonant amplitude in tuned case  $\hat{q}_{\text{ref}}$ , the largest practically stable amplitudes of the LSRs are always likely to remain more than 60 % lower

<sup>2</sup> For mistuning levels stronger than  $\sigma_r > 4\%$ , the grounding stiffness of some oscillators may become very small (cf. Eq. (20)). In combination with the weak inter-sector coupling strength of  $\kappa_c = 6 \cdot 10^{-3}$  considered in the present work, the overall effective stiffness of these oscillators (against the ground and their neighboring sectors) is weak. This allows them to reach unrealistic, extremely large amplitudes, and would even cause the linear mistuned resonant amplitudes  $\hat{q}_{95}^{\text{lin}}$  (see Fig. 7) to increase again. Moreover, the mode shape of realistic structures changes significantly for strong mistuning [13]. In this case, our minimal model of a cyclic chain with a single oscillator per sector does not seem to be an appropriate simplification anymore.

than  $\hat{q}_{ref}$ . Hence, a substantial vibration mitigation effect of the VI-NESs is maintained despite the strong localization.

### 4.2.4 Influence of the mistuning level on the localization intensity

To quantify the intensity of localization, we computed the LFs of the LSRs with the highest practically stable amplitudes. Similar to what we observed for the amplitudes, the corresponding LFs also increase with the mistuning level  $\sigma_r$ ,

as shown by the shaded regions in Fig. 8b, d, and f. The latter indicate the range in which the LFs were in 90 % of all MCSs where practically stable LSRs were found, for excitation wavenumbers  $k_0 = 0$ ,  $k_0 = 2$ , and  $k_0 = 5$ , respectively. We note that this monotonic increase of the LFs arises, since the localization intensity of host structure’s linear modes becomes higher when the mistuning level  $\sigma_r$  is increased [6]. However, there are two important differences between the localization intensity of the host structure’s linear modes and LSRs. First, the LFs of LSRs already reach high val-

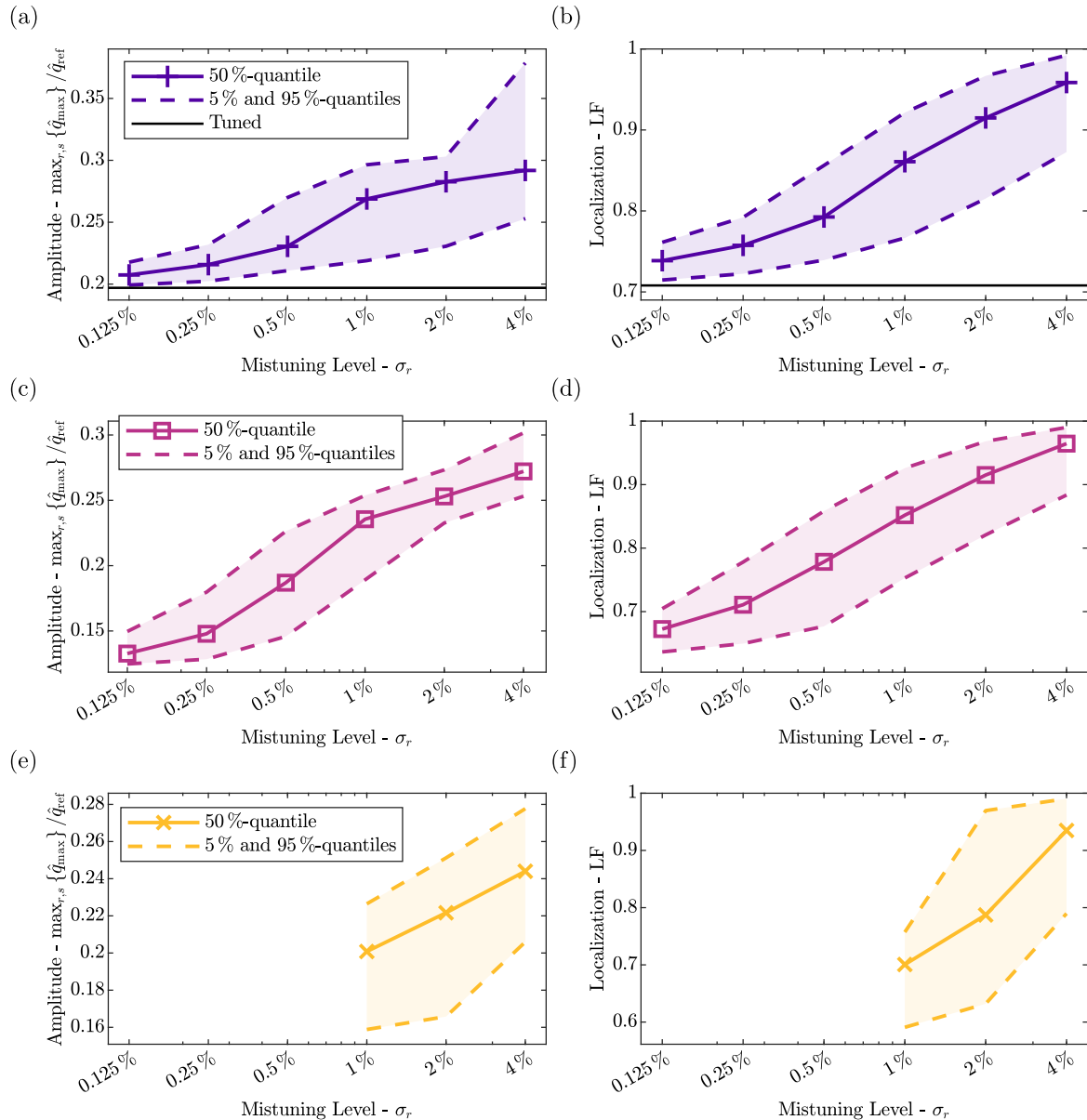


**Fig. 8** Largest practically stable amplitudes  $\max_{r,s} \{\hat{q}_{max}\}$  (left) and the corresponding LFs (right), depending on the EM mistuning level  $\sigma_r$ , for excitation wavenumbers (a,b)  $k_0 = 0$ , (c,d)  $k_0 = 2$ , and (e,f)  $k_0 = 5$ . The solid lines indicate the empirical 50%-quantile and the

shaded region shows the range between the 5 %-quantile (lower dashed line) and 95 %-quantile (upper dashed line) in which the corresponding amplitudes or LFs were in 90 % of all MCSs where practically stable LSRs were found

ues in the limiting case of a tuned system (cf. Table 2). The LFs of the host structure's linear modes, on the other hand, would always start at LF = 0 in the tuned case, where all mode shapes are of the standing/traveling wave form in Eq. (14). The second difference is that the increase of the localization intensity in the case of LSRs correlates with an increasing practically stable amplitude, whereas the resonant amplitudes of linear systems start to decrease again for large mistuning levels  $\sigma_r$  (cf. Fig. 7). For the highest considered mistuning level of  $\sigma_r = 4\%$ , the LFs of LSRs reach likely values of around LF  $\approx 0.9 \dots 1$ , as indicated by the 50%-quantiles (solid lines) in Fig. 8b, d, and f, independent of the excitation wavenumber  $k_0$ . This implies that the largest practically stable amplitudes (that are also observed for high mistuning levels  $\sigma_r$ ) occur when the energy is almost entirely confined in the single synchronized sector. From a practical perspective, this is undesired as it may locally accelerate damage mechanisms related to material fatigue. Hence, if one aims to minimize strong localization due to the interaction between LSRs and EM, the mistuning level  $\sigma_r$  should be as low as possible. In other words, the host structure should be "as tuned as possible". For high excitation wavenumbers  $k_0$ , this might even rule out the existence of practically stable LSRs entirely (see Fig. 6). We also emphasize that the benefit obtained by reducing the mistuning level  $\sigma_r$  in the case of LSRs may contradict its effect on mistuning in linear systems, where lowering the mistuning level  $\sigma_r$  can result in increasing resonant amplitudes [10], due to the appearance of the maximum shown in Fig. 7.

## 5 Clearance mistuning

We now investigate the case of CM for which we consider all local eigenfrequencies to be tuned, i.e.,  $\delta_r = \mathbf{0}$ . This implies that the *effective mistuning* of the structure now solely depends on the effective change of the synchronized sector's local eigenfrequency due to its locally acting, strong impact nonlinearity, instead of being additionally superimposed with  $\delta_r$ . Nevertheless, CM still affects the effective mistuning of the structure as the nonlinearity in the synchronized sector, and thus the effective change of its eigenfrequency, depends on its clearance  $\Gamma(1 + \delta_{\Gamma,s})$ . Due to the rare occurrence of impacts in the non-synchronized sectors, their local eigenfrequencies remain mostly unaffected.

### 5.1 Identification of possible effects on LSRs

As already seen in the derivation of the FRS in Section 3, CM does not influence the shape of the FRS itself but only the size of the clearance at which the frequency-amplitude curve is evaluated. Thereby, the value of the clearance only depends on the clearance mistuning in the synchronized sector itself,

i.e.,  $\delta_{\Gamma,s}$  (see Eq. (32)), and not on the clearance mistuning in the non-synchronized sectors  $\delta_{\Gamma,j \neq s}$ . For the mistuning levels considered in the present work,  $0 < \sigma_\Gamma \leq 4\%$ , this only results in a minimal shift of the level curve along the FRS compared to the tuned case. This causes the isolated frequency-amplitude curves to contract (expand) if the mistuned clearance is larger (smaller), i.e.,  $\delta_{\Gamma,s} > 0$  ( $\delta_{\Gamma,s} < 0$ ), than its nominal value. To illustrate this, a representative example of the FRS for excitation wavenumber  $k_0 = 1$  is shown in Fig. 9a, where the solid black line indicates the frequency-amplitude curve at the considered nominal clearance (see Table 1), and the dashed black lines show those of a CM of  $\delta_{\Gamma,s} = \pm 1\%$  in the synchronized sector. We note that the FRS in Fig. 9a is equivalent to that of the tuned case depicted in Fig. 4. When compared to the strong influence of EM on the shape of the FRS at the same mistuning level (see Fig. 4 for  $\sigma_r = 1\%$ ), the influence of CM appears to be almost negligible. This becomes even more pronounced in the particular case of the highest excitation wavenumber  $k_0 = 5$ . Here, EM was able to push the local maximum of the FRS that forms the frequency-amplitude curve around the LSRs' lowest resonance frequency past the size of the nominal clearance, which allowed for the formation of practically stable LSRs. In order to obtain a similar effect due to CM, the mistuning in the synchronized sector,  $\delta_{\Gamma,s}$ , would need to be strong enough to shift the value of the clearance into the range where this local maximum exists. In our system, this means that CM would need to reduce the size of the clearance from its nominal value of  $\Gamma = 0.33 \cdot \hat{q}_{\text{ref}}$  to a value smaller than  $\Gamma(1 + \delta_{\Gamma,s}) < 0.265 \cdot \hat{q}_{\text{ref}}$  in at least one sector. This requires a relative mistuning of  $\delta_{\Gamma,s} < -0.196$ . However, even for the highest considered mistuning level of  $\sigma_\Gamma = 4\%$ , the probability for this to occur is around  $5 \cdot 10^{-7}$ , which is negligibly small.

While it is already clear that CM alone does not lead to strong interactions with LSRs like EM, it still slightly extends the range of practically stable amplitudes, if the LSRs' frequency-amplitude curve around their lowest resonance already exists in the tuned system. This is shown by the gray point cloud in Fig. 9 which, analogous to Fig. 5, depicts the practically stable LSRs with the synchronized sector  $s$  that results in the largest practically stable amplitude based on  $N_{\text{MCS}} = 1000$  MCSs. In this example, the excitation wavenumber was  $k_0 = 1$  and we used a mistuning level of  $\sigma_\Gamma = 1\%$ . For reference, the corresponding frequency-amplitude curve of the tuned system's LSR is shown in blue, along with its practically stable range that is indicated by green stars. Even though LSRs reach slightly higher practically stable amplitudes in the presence of CM, the localization intensity, as measured by the LF, remains close to that of the tuned system's LSRs (cf. Table 2). This can be attributed to the absence of an intrinsic localization

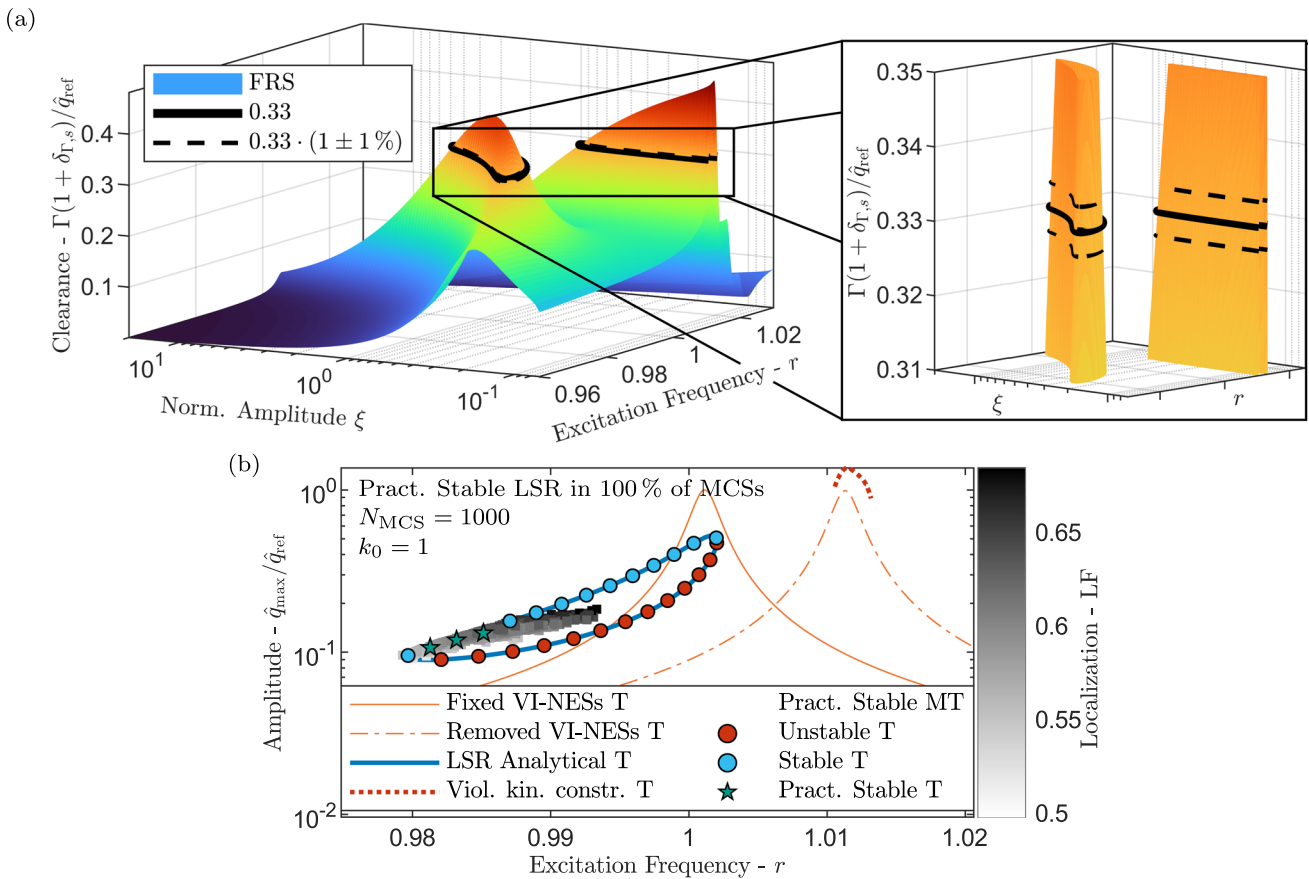


**Fig. 9** (a) Frequency response surface (FRS) of the locally synchronized response (LSR) with a single synchronized sector for excitation wavenumber  $k_0 = 1$  in the system under CM. The chosen value of the

nominal clearance  $\Gamma = 0.33 \cdot \hat{q}_{ref}$  is indicated by the solid black line. (b) shows the practical stability analysis for a mistuning level of  $\sigma_\Gamma = 1\%$

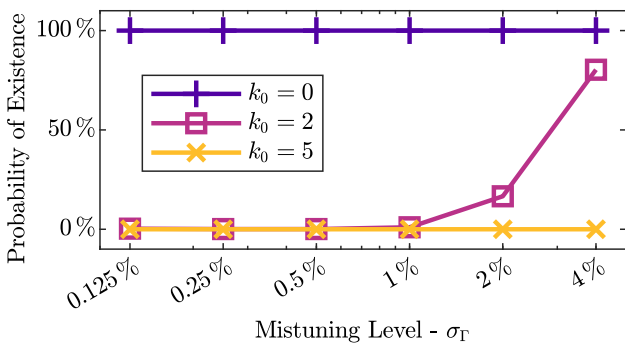


**Fig. 10** Probability that a practically stable LSR exists for at least one single synchronized sector  $s \in \{1, \dots, N_s\}$ , depending on the CM mistuning level  $\sigma_\Gamma$

of the host structure’s linear modes, which are unaffected by CM.

### 5.2 Influence of the mistuning level

In the case of excitation wavenumber  $k_0 = 0$ , where practically stable LSRs exist in the tuned system, they also always

exist in the presence of CM. This is shown by the 100% probability that a practically stable LSR exists for at least one synchronized sector  $s \in \{1, \dots, N_s\}$  at various mistuning levels  $\sigma_\Gamma$  in Fig. 10, which was estimated based on  $N_{MCSs} = 1000$  random realizations of mistuning patterns  $\delta_\Gamma$ . Hence, CM does not lead to destructive interactions with LSRs. Instead, if the mistuning level  $\sigma_\Gamma$  is high enough, it can also have a constructive, stabilizing effect if the LSRs’ frequency-amplitude curve around the lowest possible resonance already exists in the tuned case but does not exhibit practically stable solutions. This can be observed for excitation wavenumber  $k_0 = 2$  in Fig. 10, which shows that the probability that a practically stable LSRs exists increases up to 80% for the highest considered mistuning level of  $\sigma_\Gamma = 4\%$ . Based on the previous discussion on how unlikely it is that CM creates the necessary frequency-amplitude curves for excitation wavenumber  $k_0 = 5$ , it is evident why the probability for the existence of practically stable LSRs remains at 0%, even as the number of MCSs was increased to  $N_{MCS} = 5000$ . The maximum practically stable amplitudes  $\max_{r,s} \{ \hat{q}_{max} \}$  as well as their corresponding LFs do

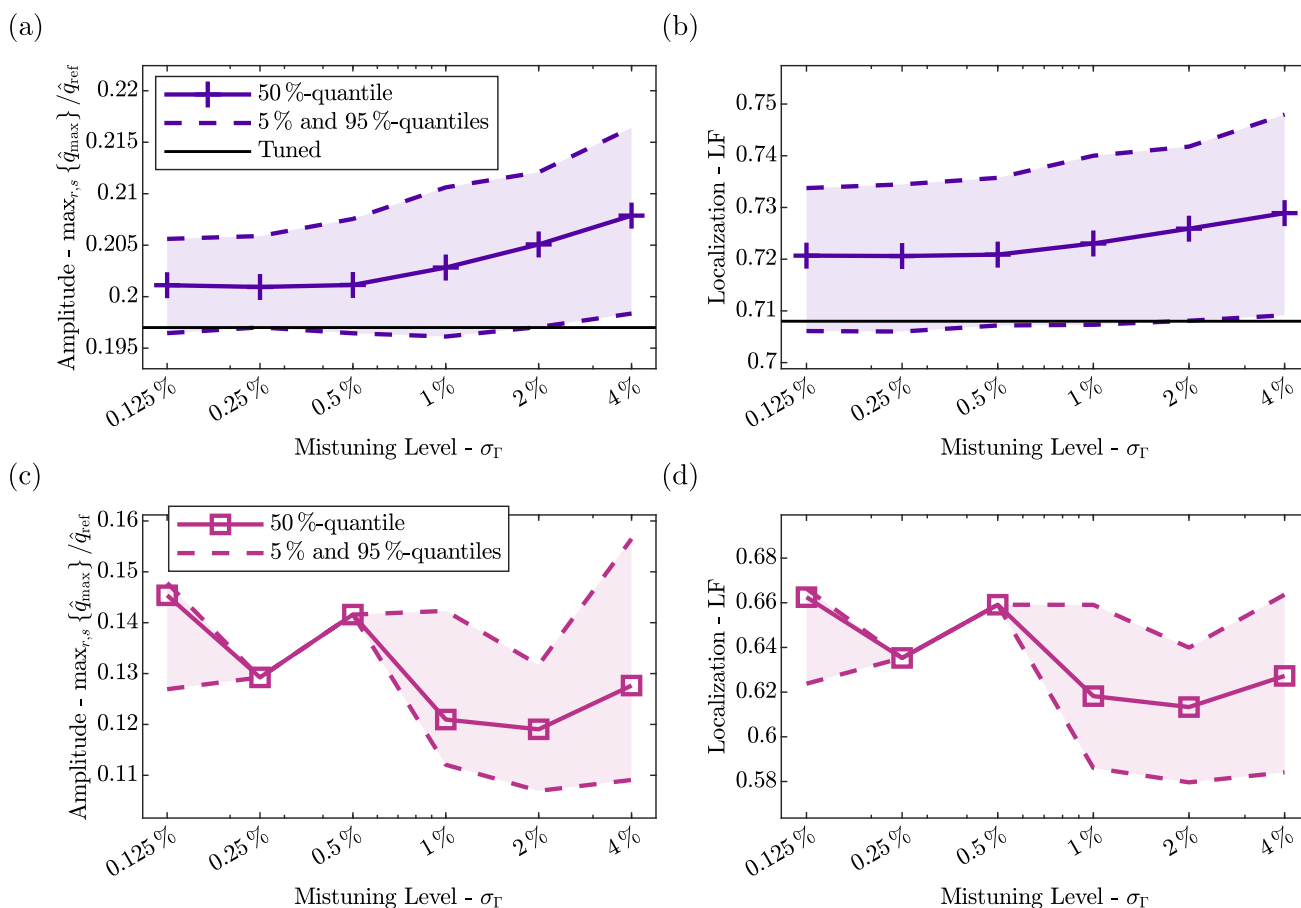


**Fig. 11** Largest practically stable amplitudes  $\max_{r,s} \{ \hat{q}_{\max} \}$  (left) and the corresponding LFs (right), depending on the CM mistuning level  $\sigma_T$ , for excitation wavenumbers (a,b)  $k_0 = 0$  and (c,d)  $k_0 = 2$ . The solid lines indicate the empirical 50 %-quantile and the colored region

shows the range between the 5 %-quantile (lower dashed line) and 95 %-quantile (upper dashed line) in which the corresponding amplitude or LF was within 90 % of all MCSs where a practically stable LSR was found

not exhibit a strong dependence on the mistuning level  $\sigma_T$ . This is indicated by the ranges in which these measures were within 90 % of all MCSs where practically stable LSRs were found (shaded regions), that are depicted in Fig. 11a and b for excitation wavenumber  $k_0 = 0$ , and in Fig. 11c and d for  $k_0 = 2$ . For excitation wavenumber  $k_0 = 0$ , even the upper bounds of these ranges, i.e., the empirical 95 %-quantiles of these measures, are only slightly higher than in the tuned case (horizontal black line). This also means that the largest practically stable amplitudes remain significantly below the linear resonant amplitude of the tuned system  $\hat{q}_{\text{ref}}$ . The same applies to the practically stabilized LSRs for excitation wavenumber  $k_0 = 2$ . We note that the “noisy” appearance of the likely ranges of amplitudes and LFs for excitation wavenumber  $k_0 = 2$  is caused by the very few random realizations of the mistuning pattern  $\delta_T$  that even led to practically stable LSRs (cf. Fig. 10).

Given the almost negligible effect of CM compared to that of EM, an analysis of their combined effect is omitted in the present work. Here, we simply expect a superposition of

the reported effects from EM and CM. In particular, we only expect slightly higher amplitudes and LFs compared to those reached for pure EM (see Fig. 8). Nevertheless, it should be emphasized that no typical mistuning levels for CM  $\sigma_T$  are known from real-world applications. Hence, it could generally be possible that realistic mistuning levels of CM will reach much higher values than those considered in the present work; these could also exceed typical mistuning intensities of EM  $\sigma_r$  that commonly fall within the low single-digit percent range [75–77]. While this does not change the qualitative interaction effects/mechanisms with LSRs that we reported herein, one should keep in mind that CM may *not always* be negligible compared to EM.

### 6 Conclusions

In the present work, we studied the interaction between Anderson localization due to mistuning and nonlinear localization in the form of Chimera-like locally synchronized

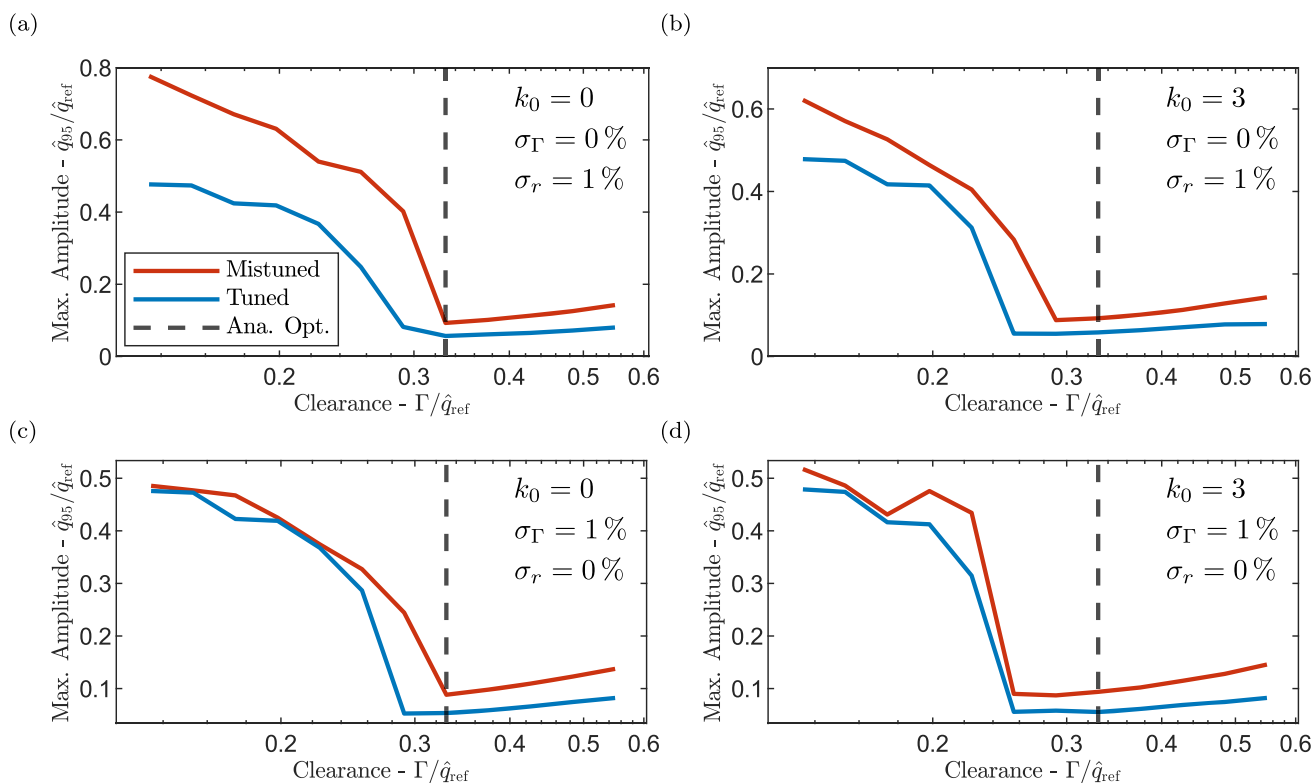


**Fig. 12** Resonant amplitude reduction for various clearances  $\Gamma$  for the inter-sector coupling strength  $\kappa_c = 6 \cdot 10^{-3}$ . The dashed black line shows the analytically estimated clearance with the strongest amplitude reduction, derived in [55]

responses (LSRs) in a harmonically forced cyclic chain of oscillators, incorporating a distributed array of VI-NESs. The system’s nominal parameters were chosen based on the study of the optimal design of the tuned system by Weidemann et al. [55], and mistuning was introduced in the form of random perturbations to the sectors’ local (uncoupled) linear eigenfrequencies (EM) or the VI-NESs’ clearances (CM).

### 6.1 Possible interaction effects

We found that even small levels of EM lead to strong changes of the LSR’s frequency response surface (FRS). Consequently, EM can create new and/or shift existing frequency-amplitude curves across a wide range of excitation frequencies. This makes it practically impossible to estimate their location *a priori*, i. e., without knowing the specific mistuning realization of the system. Moreover, it is important to note that EM can lead to the formation of practically stable LSRs in parameter ranges where LSRs would not exist in the tuned system. In the study on the tuned system [55] it was concluded that LSRs can be ignored in the design process of VI-NESs if the excitation wavenumber is moderate to high. This is because the tuned system only exhibits practically stable LSRs for the lowest few excitation wavenumbers [55]. In the presence of EM, however, practically stable

LSRs can appear in the entire range of possible excitation wavenumbers. This implies that LSRs should, in fact, *always* be considered when designing VI-NESs for an application in a real rotationally periodic structure. CM generally shows much weaker interaction effects with LSRs as it only affects the clearance at which the frequency-amplitude curve is evaluated from the FRS, but does not alter the shape of the FRS itself. More specifically, at moderate levels of CM it can be expected that the isolated frequency-amplitude curve only slightly expands or contracts compared to the configuration with nominal clearances. It should also be emphasized that both EM and CM did not yield destructive interaction effects, meaning that they did neither lead to the complete disappearance of LSRs, nor did they lower the maximum amplitude or localization level compared to the tuned system. Instead, the constructive interaction effects only increased in the considered range of mistuning levels. When intending to apply VI-NESs to real rotationally periodic systems one should thus aim to reduce any form of mistuning as much as possible. This especially applies to parameters that directly influence the linear modes of the host structure, given the almost negligible effects of CM compared to EM. The latter can be attributed to the different ways that CM and EM affect the structure’s *effective mistuning*. While EM is an independent mechanism that directly changes all sectors’ local eigenfrequencies, CM

only indirectly affects the local eigenfrequencies of the synchronized sectors by changing the intensity of their local impact nonlinearity.

## 6.2 Implications for vibration mitigation

Despite the potentially strong interactions between nonlinearly localized LSRs and Anderson localization due to mistuning, the highest amplitudes we observed were still lower than the corresponding linear resonant amplitude of the tuned system. Thus, it can be concluded that the VI-NESs still have a high potential for resonant vibration mitigation in rotationally periodic engineering structures. It should be noted that the effects of EM and CM on the (resonant) vibration level of other solutions, in particular globally synchronized responses (GSRs) and strongly modulated responses (SMRs, see Section 1.3.2) [55], were not directly considered and would be an interesting step for future work. However, we note that the highest amplitudes of LSRs reported throughout the present work are always higher than those observed in the brief study on the VI-NESs' optimal design point, presented in Appendix A, where we attempted to estimate the host structure's maximum vibration level without a particular focus on LSRs. It should also be kept in mind that the results presented in the present work are based on a minimal model of a rotationally periodic structure with VI-NESs. Since only a single oscillator per sector was considered, inter-modal targeted energy transfer (IMTET) among different mode families was completely suppressed but will be addressed in future work.

## 6.3 Transfer to other types of NESs

As already mentioned at the beginning of this article, we believe that our results may also extend to other types of NESs applied to rotationally periodic structures. This is because the resonance capture of the NESs' dynamics onto a slow invariant manifold (SIM) in a subset of sectors, or maybe onto distinct branches of a SIM in different sectors as for common "S-shaped" SIMs (see cubic NES in [33]), seems to be a nonlinear localization mechanism that is generally possible for all types of NESs [29]. Hence, nonlinearly localized responses and their interaction with mistuning should always be accounted for when applying NESs to rotationally periodic systems. Lastly, it should be noted that only the loss of (our definition of) practical stability prevents the LSR (in our system with VI-NESs) to reach detrimental localized amplitude levels, especially in the presence of mistuning. As this stability-loss mechanism is unique to the VI-NES, it remains an open question if and to what extent similar mechanisms exist for other types of NESs applied to rotationally periodic structures. A direct investigation of our hypotheses regarding

the generalization of our findings to other types of NESs is left for future work.

## Appendix A Robustness of the optimal clearance

To show the robustness of the approximate optimal clearance of the tuned system, i. e.,  $\Gamma = 0.33 \cdot \hat{q}_{\text{ref}}$ , we considered the representative examples of either pure EM or pure CM at a mistuning level of  $\sigma_r = 1\%$  or  $\sigma_\Gamma = 1\%$ , respectively, and various nominal clearances  $\Gamma$ . At each considered nominal clearance  $\Gamma$ , we generated multiple random realizations of mistuning patterns,  $\delta_r$  or  $\delta_\Gamma$ , based on Monte-Carlo simulations (MCSs). For each generated mistuning pattern, we then performed the sine-frequency-stepping procedure that was originally proposed in [50] to estimate the resonant amplitude of an isolated structure with VI-NES, and that was applied to the tuned version of the considered system in [55]. We applied the procedure as described in the following steps.

1. Specify the initial conditions by generating a uniformly distributed random displacement of all oscillators, i. e.,  $q_j(0) \in \hat{q}_{\text{ref}} [-10^{-4}, 10^{-4}]$ , placing all VI-NESs close to the left cavity wall,  $q_{a,j}(0) = q_j(0) - 0.99 \cdot \Gamma(1 + \delta_{\Gamma,j})$ , and initializing all coordinates at rest  $u_j(0) = u_{a,j}(0) = 0$ .
2. Determine the excitation frequencies with the largest maximum amplitude  $\hat{q}_{\text{max}}$  in the linear cases with fixed and removed VI-NESs,  $r_{\text{fix}}$  and  $r_{\text{rem}}$ , respectively.
3. Numerically simulate the system's transient response with a length of  $N_{\text{tr}} = \left\lceil \frac{r \ln(1000)}{2\pi r_0 D_0} \right\rceil$  excitation periods for the initial excitation frequency of  $r = 0.98 \cdot r_{\text{fix}}$ .
4. After reaching a steady state, simulate a sine-frequency stepping at 50 equidistantly-spaced excitation frequencies in the interval  $r \in [0.98 \cdot r_{\text{fix}}, 1.03 \cdot r_{\text{rem}}]$  with 300 excitation periods for each frequency. Since the frequency steps are small, introducing an additional wait time for transients after each step was found to have no effect on the extracted amplitude measures and is thus not implemented.
5. Extract the largest maximum amplitude over all excitation frequencies  $\max_r \{ \hat{q}_{\text{max}} \}$ .

The random initial displacement in step 1 is adopted according to the implementation for the tuned system in [55]. Therein, it was necessary to break any potential symmetry in the initial conditions to avoid simulating practically unstable symmetric SMRs that would otherwise occur due to an orthogonality between the measure of contact percussions  $d\Pi$  (cf. Eq. (10)) and certain mode shapes. To stay consistent with the estimation procedure between the tuned and mis-

tuned configurations, we break the initial symmetry for the mistuned system as well. The length of the transient response in step 3 is estimated from linear theory as the time after which the linear homogeneous solution of the tuned system’s fundamental mode (wavenumber  $l = 0$ ) with fixed VI-NESs would have decayed by 99.9%. It should be noted that it cannot be controlled from what type of response, i. e., GSR, SMR, or LSR (see Section 1.3.2), the maximum amplitude in step 5 is extracted. In fact, we believe that this procedure is well-suited to provide an overview over the attainable mistuned vibration levels, without putting a special emphasis on LSRs. As a scalar statistical measure of the vibration level for each nominal clearance  $\Gamma$ , we determine the empirical 95 %-quantile of the highest amplitude  $\max_r \{ \hat{q}_{\max} \}$  found during the sine-frequency-stepping over all MCSs, which we denote by  $\hat{q}_{95}$ . The resulting amplitudes  $\hat{q}_{95}$  for various sizes of the clearances  $\Gamma$  are shown by the red lines in Fig. 12 for either pure EM or CM in the cases of excitation wavenumbers  $k_0 = 0$  (standing wave excitation) or  $k_0 = 3$  (traveling wave excitation). For reference, the (deterministic) amplitudes of the tuned system are shown in blue and the dashed vertical line depicts the analytically estimated optimum at  $\Gamma = 0.33 \cdot \hat{q}_{\text{ref}}$ . Based on a statistical convergence study,  $N_{\text{MCS}} = 6500$  and  $N_{\text{MCS}} = 5000$  MCSs were performed to determine the empirical 95 %-quantiles  $\hat{q}_{95}$  for  $k_0 = 0$  and  $k_0 = 3$ , respectively. In all considered cases, the chosen nominal clearance of  $\Gamma = 0.33 \cdot \hat{q}_{\text{ref}}$  delivers a good approximation of the clearance with the strongest amplitude reduction, even in the mistuned case.

### Appendix B Local asymptotic stability analysis

To determine the local asymptotic stability of the LSRs, we interpret solutions of the HB system in Eq. (25) as fixed points of the *slow flow* equations derived with Manevitch’s complexification averaging (CX-A) technique [74]:

$$2ir\mathbf{M} \frac{d\hat{\mathbf{Q}}}{d\tau} = \hat{\mathbf{F}}_{k_0} - \hat{\mathbf{\Pi}}(\hat{\mathbf{Q}}, r, \mathcal{S}) - \mathbf{S}(r)\hat{\mathbf{Q}}. \tag{B.1}$$

Herein, the complex amplitudes  $\hat{\mathbf{Q}}$  are defined in a wider sense as the slow amplitude and phase modulation of a fast harmonic oscillation:  $\hat{\mathbf{Q}} = \hat{\mathbf{Q}}(\tau)$ . For the local asymptotic stability analysis, the system of complex ordinary differential equations in Eq. (B.1) is first transformed into a system of real ordinary differential equations that governs the dynamics of the real amplitudes  $\hat{q}_j$  and phases  $\gamma_j$ . To this end, we first write out Eq. (B.1) component-wise and substitute the relations  $\hat{Q}_j = \hat{q}_j e^{i\gamma_j}$  and  $\frac{d\hat{Q}_j}{d\tau} = \left( \frac{d\hat{q}_j}{d\tau} + i\hat{q}_j \frac{d\gamma_j}{d\tau} \right) e^{i\gamma_j}$  to arrive at:

$$\frac{i}{\alpha} \left( \frac{d\hat{q}_j}{d\tau} + i\hat{q}_j \frac{d\gamma_j}{d\tau} \right) e^{i\gamma_j} = \begin{cases} \hat{F}_{k_0,j} + \frac{8\epsilon_a r^2 \hat{q}_{a,j}}{\pi^2 \hat{q}_j} e^{i(\gamma_j - \Delta_j)} \\ - \sum_{m=1}^{N_s} S_{jm} \hat{q}_m e^{i\gamma_m} & \text{if } j \in \mathcal{S} \\ \hat{F}_{k_0,j} - \sum_{m=1}^{N_s} S_{jm} \hat{q}_m e^{i\gamma_m} & \text{if } j \notin \mathcal{S} \end{cases} \tag{B.2}$$

Herein, we also introduced the additional auxiliary variable  $\alpha = \frac{1}{2(1-\epsilon_a)r}$ . To split Eq. (B.2) into its real and imaginary part, we apply the kinematic relations of the VI-NES and its host oscillator derived in [71]:

$$e^{-i\Delta_j} = \underbrace{\frac{\hat{q}_{a,j} - \Gamma(1 + \delta_{\Gamma,j})}{\hat{q}_j}}_{=\cos(\Delta_j)} - i \underbrace{\rho \frac{\hat{q}_{a,j}}{\hat{q}_j}}_{=\sin(\Delta_j)}. \tag{B.3}$$

Recall that  $\rho = \frac{2}{\pi} \frac{1-\epsilon_N}{1+\epsilon_N}$  is also a constant auxiliary variable. Multiplying Eq. (B.2) with  $\alpha e^{-i\gamma_j}$ , and splitting it into its real and imaginary parts, yields the slow flow equations of the real amplitudes,  $\hat{q}_j$ , and phases,  $\gamma_j$ , which are shown in Eqs. (B.4) and (B.5).

$$\frac{d\hat{q}_j}{d\tau} = \alpha \left\{ \begin{array}{l} \left. \begin{array}{l} \sin(\theta_{k_0}(j-1) - \gamma_j) - \frac{8\epsilon_a r^2 \rho \hat{q}_{a,j}^2}{\pi^2 \hat{q}_j} - rC_{jj} \hat{q}_j - \sum_{\substack{m=1 \\ m \neq j}}^{N_s} ((K_{jm} + \delta K_{jm}) \sin(\gamma_m - \gamma_j)) \\ + rC_{jm} \cos(\gamma_m - \gamma_j) \hat{q}_m \end{array} \right\} \text{if } j \in \mathcal{S} \\ \left. \begin{array}{l} \sin(\theta_{k_0}(j-1) - \gamma_j) - rC_{jj} \hat{q}_j - \sum_{\substack{m=1 \\ m \neq j}}^{N_s} ((K_{jm} + \delta K_{jm}) \sin(\gamma_m - \gamma_j)) \\ + rC_{jm} \cos(\gamma_m - \gamma_j) \hat{q}_m \end{array} \right\} \text{if } j \notin \mathcal{S} \end{array} \right. \tag{B.4}$$

$$\frac{d\gamma_j}{d\tau} = \alpha \left\{ \begin{array}{l} \left. \begin{array}{l} - \frac{\cos(\theta_{k_0}(j-1) - \gamma_j)}{\hat{q}_j} - \frac{8\epsilon_a r^2 \hat{q}_{a,j} (\hat{q}_{a,j} - \Gamma(1 + \delta_{\Gamma,j}))}{\pi^2 \hat{q}_j^2} + \\ [-r^2(1 - \epsilon_a) + K_{jj} + \delta K_{jj}] + \sum_{\substack{m=1 \\ m \neq j}}^{N_s} ((K_{jm} + \delta K_{jm}) \cos(\gamma_m - \gamma_j)) \\ - rC_{jm} \sin(\gamma_m - \gamma_j) \frac{\hat{q}_m}{\hat{q}_j} \end{array} \right\} \text{if } j \in \mathcal{S} \\ \left. \begin{array}{l} - \frac{\cos(\theta_{k_0}(j-1) - \gamma_j)}{\hat{q}_j} + [-r^2(1 - \epsilon_a) + K_{jj} + \delta K_{jj}] + \sum_{\substack{m=1 \\ m \neq j}}^{N_s} ((K_{jm} + \delta K_{jm}) \cos(\gamma_m - \gamma_j)) \\ - rC_{jm} \sin(\gamma_m - \gamma_j) \frac{\hat{q}_m}{\hat{q}_j} \end{array} \right\} \text{if } j \notin \mathcal{S} \end{array} \right. \tag{B.5}$$

To determine the local asymptotic stability of the fixed points of Eq. (B.1), i.e., the solutions of Eq. (25), we now linearize the real ordinary differential equations in Eqs. (B.4) and (B.5) around these fixed points. The fixed point is locally asymptotically stable if all eigenvalues of the resulting linearization matrix  $\mathbf{J}$  lie in the left half of the complex plane. The linearization matrix  $\mathbf{J}$  of the system of ordinary differential equations governed by Eqs. (B.4) and Eq. (B.5) is defined as:

$$\mathbf{J} = \begin{bmatrix} \frac{\partial \frac{d\hat{q}}{d\tau}}{\partial \hat{q}} & \frac{\partial \frac{d\gamma}{d\tau}}{\partial \hat{q}} \\ \frac{\partial \frac{d\hat{q}}{d\tau}}{\partial \gamma} & \frac{\partial \frac{d\gamma}{d\tau}}{\partial \gamma} \end{bmatrix}. \tag{B.6}$$

Herein, the amplitudes  $\hat{q}_j$  and phases  $\gamma_j$  are gathered in the vectors  $\hat{\mathbf{q}}$  and  $\boldsymbol{\gamma}$ , respectively. The corresponding derivatives are determined component-wise for each sub-matrix of  $\mathbf{J}$  in Eqs. (B.7)-(B.10).

$$\frac{\partial \frac{d\hat{q}_j}{d\tau}}{\partial \hat{q}_p} = \alpha \begin{cases} \left. \begin{aligned} & \frac{8\epsilon_a r^2 \rho \hat{q}_{a,j}^2}{\pi^2 \hat{q}_j^2} \\ & - \frac{16\epsilon_a r^2 \rho \hat{q}_{a,j}}{\pi^2 \hat{q}_j} \frac{\partial \hat{q}_{a,j}}{\partial \hat{q}_j} - rC_{jj} \end{aligned} \right\} & \text{if } p = j \in S \\ \left. \begin{aligned} & -rC_{jj} \end{aligned} \right\} & \text{if } p = j \notin S \\ \left. \begin{aligned} & -((K_{jp} + \delta K_{jp}) \sin(\gamma_p - \gamma_j)) \\ & + rC_{jp} \cos(\gamma_p - \gamma_j) \end{aligned} \right\} & \text{if } p \neq j \end{cases} \tag{B.7}$$

$$\frac{\partial \frac{d\hat{q}_j}{d\tau}}{\partial \gamma_p} = \alpha \begin{cases} \left. \begin{aligned} & -\cos(\theta_{k_0}(j-1) - \gamma_j) \\ & + \sum_{\substack{m=1 \\ m \neq j}}^{N_s} ((K_{jm} + \delta K_{jm}) \cos(\gamma_m - \gamma_j)) \end{aligned} \right\} & \text{if } p = j \\ \left. \begin{aligned} & -rC_{jm} \sin(\gamma_m - \gamma_j) \hat{q}_m \\ & [(K_{jp} + \delta K_{jp}) \cos(\gamma_p - \gamma_j)] \\ & - rC_{jp} \sin(\gamma_p - \gamma_j) \hat{q}_p \end{aligned} \right\} & \text{if } p \neq j \end{cases} \tag{B.8}$$

$$\frac{\partial \frac{d\gamma_j}{d\tau}}{\partial \gamma_p} = \alpha \begin{cases} \left. \begin{aligned} & -\frac{\sin(\theta_{k_0}(j-1) - \gamma_j)}{\hat{q}_j} + \\ & \sum_{\substack{m=1 \\ m \neq j}}^{N_s} ((K_{jm} + \delta K_{jm}) \sin(\gamma_m - \gamma_j)) \end{aligned} \right\} & \text{if } p = j \\ \left. \begin{aligned} & + rC_{jm} \cos(\gamma_m - \gamma_j) \frac{\hat{q}_m}{\hat{q}_j} \\ & - ((K_{jp} + \delta K_{jp}) \sin(\gamma_p - \gamma_j)) \\ & + rC_{jp} \cos(\gamma_p - \gamma_j) \frac{\hat{q}_p}{\hat{q}_j} \end{aligned} \right\} & \text{if } p \neq j \end{cases} \tag{B.9}$$

$$\frac{\partial \frac{d\gamma_j}{d\tau}}{\partial \hat{q}_p} = \alpha \begin{cases} \left. \begin{aligned} & \frac{\cos(\theta_{k_0}(j-1) - \gamma_j)}{\hat{q}_j^2} \\ & + \frac{16\epsilon_a r^2 \hat{q}_{a,j} (\hat{q}_{a,j} - \Gamma(1 + \delta_{\Gamma,j}))}{\pi^2 \hat{q}_j^3} \\ & \frac{8\epsilon_a r^2 (2\hat{q}_{a,j} - \Gamma(1 + \delta_{\Gamma,j}))}{\pi^2 \hat{q}_j^2} \frac{\partial \hat{q}_{a,j}}{\partial \hat{q}_j} \end{aligned} \right\} & \text{if } p = j \in S \\ \left. \begin{aligned} & \sum_{\substack{m=1 \\ m \neq j}}^{N_s} ((K_{jm} + \delta K_{jm}) \cos(\gamma_m - \gamma_j)) \\ & - rC_{jm} \sin(\gamma_m - \gamma_j) \frac{\hat{q}_m}{\hat{q}_j^2} \end{aligned} \right\} & \text{if } p = j \notin S \\ \left. \begin{aligned} & \sum_{\substack{m=1 \\ m \neq j}}^{N_s} ((K_{jm} + \delta K_{jm}) \cos(\gamma_m - \gamma_j)) \\ & - rC_{jm} \sin(\gamma_m - \gamma_j) \frac{\hat{q}_m}{\hat{q}_j^2} \\ & ((K_{jp} + \delta K_{jp}) \cos(\gamma_p - \gamma_j)) \\ & - rC_{jp} \sin(\gamma_p - \gamma_j) \frac{1}{\hat{q}_j} \end{aligned} \right\} & \text{if } p \neq j \end{cases} \tag{B.10}$$

Note that  $\hat{q}_{a,j}$  is related to  $\hat{q}_j$  through Eq. (28). Moreover, Eqs. (B.7) and (B.10) utilize the derivative of the stable branch of the SIM:

$$\frac{\partial \hat{q}_{a,j}}{\partial \hat{q}_j} = \frac{\hat{q}_j}{\sqrt{(1 + \rho^2) \hat{q}_j^2 - (\rho\Gamma)^2 (1 + \delta_{\Gamma,j})^2}}, \tag{B.11}$$

$$\hat{q}_j > \frac{\rho\Gamma(1 + \delta_{\Gamma,j})}{\sqrt{1 + \rho^2}}.$$

### Appendix C Number of possibly coexisting LSRs

For each specific random realization of mistuning patterns,  $\delta_r$  and  $\delta_\Gamma$ , multiple LSRs may possibly coexist. In other words, depending on the initial conditions of the EOMs in Eqs. (9) and (10), it may be possible to reach various different steady-states with different permutations of synchronized and non-synchronized sectors. To quantify the number of possibly coexisting LSRs,  $N_{\text{LSR}}$ , we exploit that we can uniquely characterize an LSR by its set of synchronized sectors  $S$ . Hence, to count the number of LSRs that may possibly coexist, we can count how many unique sets  $S$  exist for a given number of sectors  $N_s$ . To this end, we consider that each sector  $j$  can either be included in  $S$  or not, i.e., it can either be synchronized or not. This reduces the problem of counting the number of possibly coexisting LSRs to a simple permutation problem (two possible states for each sector) with the solution:

$$N_{\text{LSR}} = 2^{N_s} - 2. \tag{C.1}$$

The subtraction of two excludes the special cases where either all sectors are synchronized, i.e.,  $\mathcal{S} = \{1, \dots, N_s\}$  (GSR), or where no sector is synchronized, i.e.,  $\mathcal{S} = \emptyset$ . We note that this way of counting the number of possibly coexisting LSRs,  $N_{\text{LSR}}$ , does not account for the coexistence of solutions with the same set of synchronized sectors  $\mathcal{S}$ , e.g., due to isolated or overhanging branches. Moreover, it should be emphasized that the expression in Eq. (C.1) only counts the number of *possibly* coexisting LSRs which may be higher than the number of kinematically admissible and (practically) stable coexisting LSRs. In fact, it was already shown in [55] that LSRs only exist in a finite range of clearances  $\Gamma$ . Counting the number of (actually) coexisting LSRs for a given realization of the system would require one to systematically analyze all  $N_{\text{LSR}}$  possibly coexisting LSRs first, e.g., by means of the analytical model presented herein.

The number of possibly coexisting LSRs,  $N_{\text{LSR}}$ , in the mistuned system given in Eq. (C.1), differs from the expression we derived for the tuned system in our previous study [55]. In the latter, we regarded all LSRs whose sets of synchronized sectors  $\mathcal{S}$  were circularly shifted versions of one another as the same solution<sup>3</sup>, given that the tuned system possesses ideal cyclic symmetry. A circular shift can be achieved by adding the same but arbitrary integer number to all indices of the synchronized sectors contained in  $\mathcal{S}$ , under consideration of the periodic boundary conditions in Eq. (8). This has the same effect as redefining the arbitrary choice of which of the tuned system’s identical sectors is the “first” sector  $j = 1$ . Under these considerations, the number of possibly coexisting LSRs in the tuned system was given in [55] as the solution to the Necklace Counting permutation problem,  $N_{\text{LSR}} = \left(\frac{1}{N_s} \sum_{n=1}^{N_s} 2^{\text{gcd}(n, N_s)}\right) - 2$ , where  $\text{gcd}(\square, \square)$  is the greatest common divisor. For a derivation of this expression, we refer the interested reader to a combinatorics textbook [78]. It is obvious that the choice of the *mistuned* system’s first sector  $j = 1$  matters in this context as all sectors are slightly different (mistuned). Hence, even LSRs with circularly shifted sets of synchronized sectors  $\mathcal{S}$  are counted as separate solutions in Eq. (C.1), and the number of possibly coexisting unique LSRs in the mistuned system is larger than in the tuned system. This is a first indication of the drastic increase in complexity one has to expect when accounting for mistuning in the design of a cyclic structure with VI-NESs. In the case of  $N_s = 10$  sectors (cf. Table 1), the tuned system possesses  $N_{\text{LSR}} = 106$  possibly coexisting unique LSRs [55], whereas the mistuned system possesses  $N_{\text{LSR}} = 1022$  possi-

bly coexisting unique LSRs for *each* realization of mistuning patterns  $\delta_r$  and  $\delta_\Gamma$ .

### Appendix D Representative mistuning pattern used in Fig. 4

**Table 3** Normalized representative eigenfrequency mistuning pattern  $\delta_r^*$  with a spatial corrected sample standard deviation of unity. All values are rounded to the sixth decimal place

|                  |           |                   |           |
|------------------|-----------|-------------------|-----------|
| $\delta_{r,1}^*$ | 0.984382  | $\delta_{r,6}^*$  | 0.852898  |
| $\delta_{r,2}^*$ | -0.410474 | $\delta_{r,7}^*$  | 0.574996  |
| $\delta_{r,3}^*$ | -0.735182 | $\delta_{r,8}^*$  | 0.231832  |
| $\delta_{r,4}^*$ | 1.478324  | $\delta_{r,9}^*$  | -1.719885 |
| $\delta_{r,5}^*$ | -0.256372 | $\delta_{r,10}^*$ | -1.000519 |

### Appendix E Frequency region with practically stable solutions

In the following, we demonstrate that practically stable solutions only occur below the lowest resonance of the LSR, based on a representative example for excitation wavenumber  $k_0 = 1$  and a mistuning level of  $\sigma_r = 1\%$ . To this end, we momentarily fix the (nominal) clearance at a smaller value of  $\Gamma = 0.08 \cdot \hat{q}_{\text{ref}}$  where the LSR covers a larger frequency range and the qualitative differences are more clearly visible. The resulting frequency-amplitude curve for the synchronized sector,  $\hat{q}_s$ , is shown in Fig. 13 by the dashed gray line. As a reference, the solid and dashed-dotted orange line in the background indicate the linear frequency-amplitude curves of the tuned system with fixed or removed VI-NESs, respectively. The blue line indicates the maximum amplitude,  $\hat{q}_{\text{max}}$ , and transitions to a red-dotted line when the kinematic constraint is violated. As already reported for the tuned system in [55], the maximum amplitude  $\hat{q}_{\text{max}}$  does not necessarily coincide with the amplitude in the synchronized sector  $\hat{q}_s$ . This was already observed for the majority of the range of excitation frequencies  $r$  past the lowest resonance of the LSR in the tuned system [55] and mostly (but not necessarily) coincides with a violation of the kinematic constraint. The stability of the solutions is indicated by their respective markers: practically stable solutions are indicated by green stars, locally asymptotically stable but practically unstable solutions are indicated by blue dots, and unstable solutions are indicated by red dots. For all practically stable solutions, the markers depict the numerically determined amplitude during the last 300 excitation periods of the simulation performed in the practical stability analysis (see Section 3.3). One can

<sup>3</sup> Strictly speaking, LSRs whose sets of synchronized sectors  $\mathcal{S}$  are circularly shifted versions of one another are still coexisting solutions of the tuned system’s EOMs. However, their qualitative dynamic behavior in terms of their stability and potential bifurcations, as well as their quantitative behavior in terms of their vibration levels is, in fact, the same.

**Fig. 13** Representative numerical stability analysis of the analytically determined frequency-amplitude branches of an LSR with synchronization in a single sector of a system configuration with EM

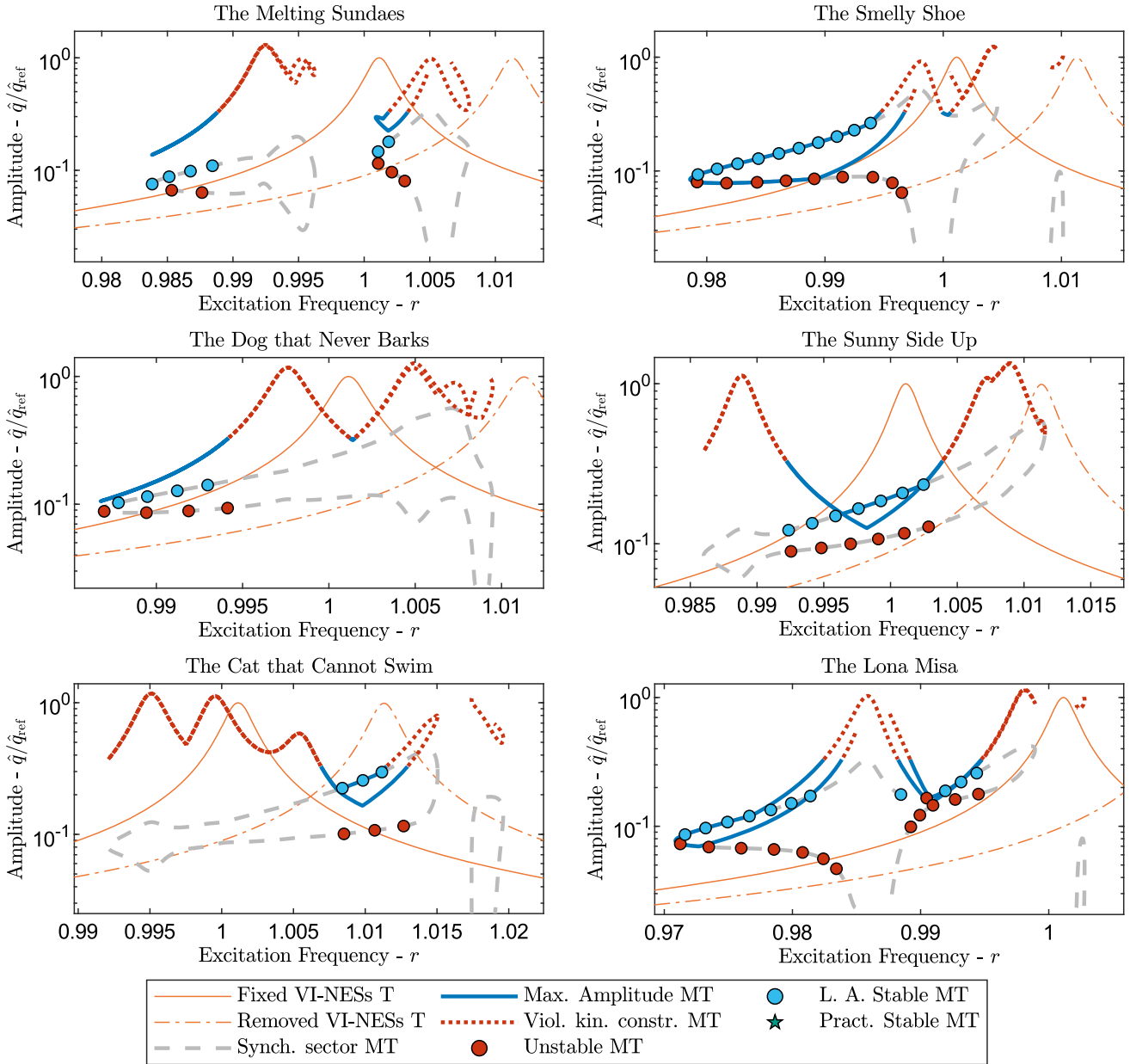
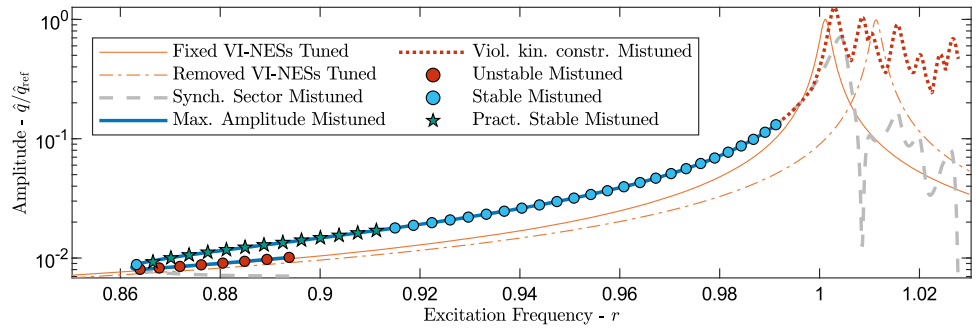


**Fig. 14** Examples of the frequency-amplitude curves and their stability of the locally synchronized response (LSR) with a single synchronized sector in the case of eigenfrequency mistuning (EM). The inter-sector coupling strength is set to  $\kappa_c = 6 \cdot 10^{-3}$  and the excitation wavenumber is  $k_0 = 1$

clearly see that practically stable solutions only appear below the lowest resonance of the LSR. It should be noted that all solutions past the lowest nonlinear resonance violate the kinematic constraint in the example shown in Fig. 13. Nevertheless, we could also not observe practically stable LSRs for other mistuning realizations that did not lead to a violation of the kinematic constraint in this frequency region.

## Appendix F A collection of art

In the case of EM, the frequency-amplitude curves of the LSR take on very “strange” shapes. Nevertheless, our analytical study of the FRS and the slow flow equations allows us to efficiently compute their shape and stability. We collected a few representative examples in Fig. 14.

**Acknowledgements** The authors acknowledge support by the state of Baden-Württemberg through the use of its high-performance computing center bwHPC. T.W. would like to thank Dr. Johann Gross for the valuable discussions on mistuning. All authors thank an anonymous reviewer for pointing out that locally synchronized responses may be viewed as Chimera-like states.

**Author Contributions** T.W.: Conceptualization, Methodology, Software, Validation, Formal analysis, Investigation, Data Curation, Writing - Original Draft, Visualization. L.A.B.: Writing - Review & Editing, Supervision. A.F.V.: Conceptualization, Writing - Review & Editing, Supervision. M.K.: Conceptualization, Resources, Writing - Review & Editing, Supervision, Funding acquisition.

**Funding** Open Access funding enabled and organized by Projekt DEAL. This work was funded by the Deutsche Forschungsgemeinschaft (DFG, German Research Foundation) [Project 514021014].

**Data Availability** The code used to generate all results is available on GitHub at ‘<https://github.com/tobiaswdm/CC>’.

## Declarations

**Competing interests** The authors declare no competing interests.

**Open Access** This article is licensed under a Creative Commons Attribution 4.0 International License, which permits use, sharing, adaptation, distribution and reproduction in any medium or format, as long as you give appropriate credit to the original author(s) and the source, provide a link to the Creative Commons licence, and indicate if changes were made. The images or other third party material in this article are included in the article’s Creative Commons licence, unless indicated otherwise in a credit line to the material. If material is not included in the article’s Creative Commons licence and your intended use is not permitted by statutory regulation or exceeds the permitted use, you will need to obtain permission directly from the copyright holder. To view a copy of this licence, visit <http://creativecommons.org/licenses/by/4.0/>.

## References

- Liu, Z., Zhang, X., Mao, Y., Zhu, Y.Y., Yang, Z., Chan, C.T., Sheng, P.: Locally resonant sonic materials. *Science* **289**, 1734–1736 (2000)
- Hussein, M.I., Leamy, M.J., Ruzzene, M.: Dynamics of phononic materials and structures: Historical origins, recent progress, and future outlook. *Appl. Mech. Rev.* **66**, 040802 (2014)
- McDaniel, T., Chang, K.: Dynamics of rotationally periodic large space structures. *J. Sound Vib.* **68**, 351–368 (1980)
- Rao, J.S.: *Turbomachine Blade Vibration*. New Age International, (1991)
- Anderson, P.W.: Absence of diffusion in certain random lattices. *Phys. Rev.* **109**, 1492–1505 (1958)
- Wei, S.-T., Pierre, C.: Localization phenomena in mistuned assemblies with cyclic symmetry part i: Free vibrations. *J. Vib. Acoust.* **110**, 429–438 (1988)
- Pierre, C., Cha, P.D.: Strong mode localization in nearly periodic disordered structures. *AIAA J.* **27**, 227–241 (1989)
- Hodges, C.: Confinement of vibration by structural irregularity. *J. Sound Vib.* **82**, 411–424 (1982)
- Wei, S.-T., Pierre, C.: Localization phenomena in mistuned assemblies with cyclic symmetry part ii: Forced vibrations. *J. Vib. Acoust.* **110**, 439–449 (1988)
- Castanier, M.P., Pierre, C.: Consideration on the benefits of intentional blade mistuning for the forced response of turbomachinery rotors, in *Analysis and Design Issues for Modern Aerospace Vehicles*, pp. 419–425, American Society of Mechanical Engineers, (1997)
- Ewins, D.: The effects of detuning upon the forced vibrations of bladed disks. *J. Sound Vib.* **9**, 65–79 (1969)
- Ewins, D.J., Han, Z.S.: Resonant vibration levels of a mistuned bladed disk. *J. Vib. Acoust.* **106**, 211–217 (1984)
- Castanier, M.P., Pierre, C.: Modeling and analysis of mistuned bladed disk vibration: Current status and emerging directions. *J. Propul. Power* **22**, 384–396 (2006)
- García-Mata, I., Shepelyansky, D.L.: Delocalization induced by nonlinearity in systems with disorder. *Phys. Rev. E* **79**, 026205 (2009)
- Petrov, E.P., Ewins, D.J.: Effects of damping and varying contact area at blade-disk joints in forced response analysis of bladed disk assemblies. *J. Turbomach.* **128**, 403–410 (2006)
- Charleux, D., Gibert, C., Thouverez, F., Dupeux, J.: Numerical and experimental study of friction damping blade attachments of rotating bladed disks. *Int. J. Rotating Mach.* **2006**, 1 (2006)
- Krack, M., Salles, L., Thouverez, F.: Vibration prediction of bladed disks coupled by friction joints. *Archives of Computational Methods in Engineering* **24**, 589–636 (2017)
- Petrov, E.P., Ewins, D.J.: Method for analysis of nonlinear multi-harmonic vibrations of mistuned bladed disks with scatter of contact interface characteristics. *J. Turbomach.* **127**, 128–136 (2005)
- Zhou, B., Thouverez, F., Lenoir, D.: Essentially nonlinear piezoelectric shunt circuits applied to mistuned bladed disks. *J. Sound Vib.* **333**, 2520–2542 (2014)
- Tang, W., Epureanu, B.I.: Nonlinear dynamics of mistuned bladed disks with ring dampers. *Int. J. Non-Linear Mech.* **97**, 30–40 (2017)
- Joachim, J., Nyssen, F., Batailly, A.: Numerical investigation of a mistuned academic bladed disk dynamics with blade/casing contact. *J. Eng. Gas Turbines Power* **143**, 041028 (2021)
- Quaegerbeur, S., Thouverez, F.: Mistuning sensitivity of a fan bladed-disk with geometrical nonlinearities. *J. Eng. Gas Turbines Power* **145**, 121012 (2023)
- Dauxois, T., Peyrard, M.: Energy localization in nonlinear lattices. *Phys. Rev. Lett.* **70**, 3935–3938 (1993)
- Vakakis, A., Nayfeh, T., King, M.: A multiple-scales analysis of nonlinear, localized modes in a cyclic periodic system. *J. Appl. Mech.* **60**, 388–397 (1993)
- King, M.E., Vakakis, A.F.: A very complicated structure of resonances in a nonlinear system with cyclic symmetry: Nonlinear forced localization. *Nonlinear Dyn.* **7**, 85–104 (1995)

26. Aubrecht, J., Vakakis, A.F.: Localized and non-localized nonlinear normal modes in a multi-span beam with geometric nonlinearities. *J. Vib. Acoust.* **118**, 533–542 (1996)
27. Sievers, A.J., Takeno, S.: Intrinsic localized modes in anharmonic crystals. *Phys. Rev. Lett.* **61**, 970–973 (1988)
28. Nayfeh, A.H., Mook, D.T.: *Nonlinear Oscillations*. Wiley, (1995)
29. Vakakis, A.F., Gendelman, O.V., Bergman, L.A., McFarland, D.M., Kerschen, G., Lee, Y.S.: *Nonlinear Targeted Energy Transfer in Mechanical and Structural Systems*, vol. 156. Springer Netherlands, 1 ed., (2009)
30. Vakakis, A.F., Manevitch, L.I., Mikhlin, Y.V., Pilipchuk, V.N., Zevin, A.A.: *Normal Modes and Localization in Nonlinear Systems*. Wiley, (1996)
31. Takeno, S., Homma, S.: Propagation of a soliton and a nonlinear self-localized state in a one-dimensional disordered nonlinear lattice. *J. Phys. Soc. Jpn.* **60**, 731–734 (1991)
32. King, M.E., Layne, P.A.: Dynamics of nonlinear cyclic systems with structural irregularity. *Nonlinear Dyn.* **15**, 225–244 (1998)
33. Li, T., Seguy, S., Berlioz, A.: Dynamics of cubic and vibro-impact nonlinear energy sink: Analytical, numerical, and experimental analysis. *J. Vib. Acoust.* **138**, 031010 (2016)
34. Ding, H., Chen, L.-Q.: Designs, analysis, and applications of nonlinear energy sinks. *Nonlinear Dyn.* **100**, 3061–3107 (2020)
35. Sigalov, G., Gendelman, O.V., AL-Shudeifat, M.A., Manevitch, L.I., Vakakis, A.F., Bergman, L.A.: Resonance captures and targeted energy transfers in an inertially-coupled rotational nonlinear energy sink. *Nonlinear Dyn.* **69**, 1693–1704 (2012)
36. Gendelman, O.V., Sigalov, G., Manevitch, L.I., Mane, M., Vakakis, A.F., Bergman, L.A.: Dynamics of an eccentric rotational nonlinear energy sink. *J. Appl. Mech.* **79**, 011012 (2012)
37. Avramov, K.V., Mikhlin, Y.V.: Snap-through truss as a vibration absorber. *J. Vib. Control* **10**, 291–308 (2004)
38. Qiu, D., Li, T., Seguy, S., Paredes, M.: Efficient targeted energy transfer of bistable nonlinear energy sink: application to optimal design. *Nonlinear Dyn.* **92**, 443–461 (2018)
39. Wang, J., Wierschem, N.E., Spencer, B.F., Lu, X.: Track nonlinear energy sink for rapid response reduction in building structures. *J. Eng. Mech.* **141**, 04014104 (2015)
40. Wang, J., Wierschem, N., Spencer, B.F., Lu, X.: Experimental study of track nonlinear energy sinks for dynamic response reduction. *Eng. Struct.* **94**, 9–15 (2015)
41. Farid, M.: Dynamics of a hybrid cubic vibro-impact oscillator and nonlinear energy sink. *Commun. Nonlinear Sci. Numer. Simul.* **117**, 106978 (2023)
42. Arnold, V.I.: *Dynamical Systems III*, vol. 3. Springer, Berlin Heidelberg (1988)
43. Den-Hartog, J.: *Mechanical Vibrations*. Dover Publications, (1985)
44. Farid, M., Gendelman, O.V., Babitsky, V.I.: Dynamics of a hybrid vibro-impact nonlinear energy sink. *ZAMM - Journal of Applied Mathematics and Mechanics / Zeitschrift für Angewandte Mathematik und Mechanik* **101**, e201800341 (2021)
45. Chabrier, R., Chevallier, G., Foltête, E., Sadoulet-Reboul, E.: Experimental investigations of a vibro-impact absorber attached to a continuous structure. *Mech. Syst. Signal Process.* **180**, 109382 (2022)
46. Weidemann, T., Carassale, L., Denoël, V., Krack, M.: On the broadband efficacy of impact absorbers. *J. Sound Vib.* **572**, 118161 (2024)
47. Gendelman, O.: Analytic treatment of a system with a vibro-impact nonlinear energy sink. *J. Sound Vib.* **331**, 4599–4608 (2012)
48. Nucera, F., Vakakis, A.F., McFarland, D.M., Bergman, L.A., Kerschen, G.: Targeted energy transfers in vibro-impact oscillators for seismic mitigation. *Nonlinear Dyn.* **50**, 651–677 (2007)
49. Fang, B., Theurich, T., Krack, M., Bergman, L.A., Vakakis, A.F.: Vibration suppression and modal energy transfers in a linear beam with attached vibro-impact nonlinear energy sinks. *Commun. Nonlinear Sci. Numer. Simul.* **91**, 105415 (2020)
50. Theurich, T., Krack, M.: Experimental validation of impact energy scattering as concept for mitigating resonant vibrations., *Journal of Structural Dynamics*, (2023)
51. Gendelman, O., Alloni, A.: Dynamics of forced system with vibro-impact energy sink. *J. Sound Vib.* **358**, 301–314 (2015)
52. Li, T., Seguy, S., Berlioz, A.: On the dynamics around targeted energy transfer for vibro-impact nonlinear energy sink. *Nonlinear Dyn.* **87**, 1453–1466 (2017)
53. Vakakis, A.F., Gendelman, O.V., Bergman, L.A., Mojahed, A., Gzal, M.: Nonlinear targeted energy transfer: state of the art and new perspectives. *Nonlinear Dyn.* **108**, 711–741 (2022)
54. Gzal, M.O., Gendelman, O.V., Bergman, L.A., Vakakis, A.F.: Enhanced seismic mitigation through energy management using nonlinear energy sinks with clearance–contacts, *Nonlinear Dynamics*, (2024)
55. Weidemann, T., Bergman, L.A., Vakakis, A.F., Krack, M.: Energy transfer and localization in a forced cyclic chain of oscillators with vibro-impact nonlinear energy sinks. *Nonlinear Dyn.* **113**, 14319–14360 (2025)
56. Abrams, D.M., Strogatz, S.H.: Chimera states for coupled oscillators. *Phys. Rev. Lett.* **93**, 174102 (2004)
57. Sethia, G.C., Sen, A.: Chimera states: The existence criteria revisited. *Phys. Rev. Lett.* **112**, 144101 (2014)
58. Haugland, S.W.: The changing notion of chimera states, a critical review. *Journal of Physics: Complexity* **2**, 032001 (2021)
59. Niedergesäß, B., Papangelo, A., Grolet, A., Vizzaccaro, A., Fontanela, F., Salles, L., Sievers, A., Hoffmann, N.: Experimental observations of nonlinear vibration localization in a cyclic chain of weakly coupled nonlinear oscillators. *J. Sound Vib.* **497**, 115952 (2021)
60. Moreau, J.J.: *Unilateral Contact and Dry Friction in Finite Freedom Dynamics*, pp. 1–82. Springer Vienna, (1988)
61. Glocker, C.: *Set-Valued Force Laws*. Springer, Berlin Heidelberg (2001)
62. Olson, B.J., Shaw, S.W., Shi, C., Pierre, C., Parker, R.G.: Circulant matrices and their application to vibration analysis. *Appl. Mech. Rev.* **66**, 040803 (2014)
63. Matsumoto, M., Nishimura, T.: Mersenne twister. *ACM Trans. Model. Comput. Simul.* **8**, 3–30 (1998)
64. Capobianco, G., Eugster, S.R., Leine, R.I.: Moreau-type integrators based on the time finite element discretization of the virtual action. *PAMM* **17**, 143–144 (2017)
65. Klauke, T., Kühhorn, A., Beirrow, B., Golze, M.: Numerical investigations of localized vibrations of mistuned blade integrated disks (blisks). *J. Turbomach.* **131**, 031002 (2009)
66. Whitehead, D.S.: The maximum factor by which forced vibration of blades can increase due to mistuning. *J. Eng. Gas Turbines Power* **120**, 115–119 (1998)
67. Brake, M.R.: ed., *The Mechanics of Jointed Structures*. Springer International Publishing, (2018)
68. Krack, M., Gross, J.: *Harmonic Balance for Nonlinear Vibration Problems*. Springer International Publishing, (2019)
69. Youssef, B., Leine, R.I.: A complete set of design rules for a vibro-impact nes based on a multiple scales approximation of a nonlinear mode. *J. Sound Vib.* **501**, 116043 (2021)
70. Youssef, B., Karoui, A.Y., Leine, R.I.: Asymmetric vibro-impact nonlinear energy sink with dry friction: an impact map approach, *Nonlinear Dynamics*, (2025)
71. Theurich, T., Vakakis, A.F., Krack, M.: Predictive design of impact absorbers for mitigating resonances of flexible structures using a semi-analytical approach. *J. Sound Vib.* **516**, 116527 (2022)
72. Chin, W., Ott, E., Nusse, H.E., Grebogi, C.: Grazing bifurcations in impact oscillators. *Phys. Rev. E* **50**, 4427–4444 (1994)

73. Theurich, T., Gross, J., Krack, M.: Effects of modal energy scattering and friction on the resonance mitigation with an impact absorber. *J. Sound Vib.* **442**, 71–89 (2019)
74. Manevitch, L.I.: *Complex Representation of Dynamics of Coupled Nonlinear Oscillators*, pp. 269–300. Springer US, (1999)
75. Feiner, D.M., Griffin, J.H.: Mistuning identification of bladed disks using a fundamental mistuning model-part ii: Application. *J. Turbomach.* **126**, 159–165 (2004)
76. Laxalde, D., Thouverez, F., Sinou, J.-J., Lombard, J.-P., Baumhauer, S.: Mistuning identification and model updating of an industrial blisk. *Int. J. Rotating Mach.* **2007**, 1–10 (2007)
77. Judge, J.A., Pierre, C., Ceccio, S.L.: Experimental mistuning identification in bladed disks using a component-mode-based reduced-order model. *AIAA J.* **47**, 1277–1287 (2009)
78. Sagan, B.E.: *Combinatorics : the art of counting*. American Mathematical Society, (2020)

**Publisher's Note** Springer Nature remains neutral with regard to jurisdictional claims in published maps and institutional affiliations.